Neurobiology of Disease

Pathogenic Mechanisms of Cytosolic and Membrane-Enriched α-Synuclein Converge on Fatty Acid Homeostasis

Arati Tripathi, Heba Alnakhala, Elizabeth Terry-Kantor, Andrew Newman, Lei Liu, Thibaut Imberdis, Saranna Fanning, Silke Nuber, Nagendran Ramalingam, Dennis Selkoe, and Ulf Dettmer

Ann Romney Center for Neurologic Diseases, Department of Neurology, Brigham and Women's Hospital and Harvard Medical School, Boston, Massachusetts 02115

α-Synuclein (αS) plays a key role in Parkinson's disease. Although Parkinson's disease is typically "sporadic," inherited αS missense mutations provide crucial insights into molecular mechanisms. Here, we examine two clinical mutants, E46K and G51D, which are both in the conserved N-terminus that mediates transient αS-membrane interactions. However, E46K increases and G51D decreases αS-membrane interactions. Previously, we amplified E46K via the 11-residue repeat motifs, creating "3K" (E35K+E46K+E61K). Here, we engineered these motifs to amplify G51D (V40D+G51D+V66D = "3D") and systematically compared E46K/3K versus G51D/3D. We found that G51D increased cytosolic αS in neural cells and 3D aggravates this. G51D, and 3D even more, reduced αS multimer-to-monomer (αS60:αS14) ratio. Both amplified variants caused cellular stress in rat primary neurons and reduced growth in human neuroblastoma cells. Importantly, both 3K- and 3D-induced stress was ameliorated by pharmacologically inhibiting stearoyl-CoA desaturase or by conditioning the cells in palmitic (16:0) or myristic (14:0) acid. SCD inhibition lowered lipid-droplet accumulation in both 3D- and 3K-expressing cells and benefitted G51D by normalizing multimer:monomer ratio, as reported previously for E46K. Our findings suggest that, despite divergent cytosol/membrane partitioning, both G51D and E46K neurotoxicity can be prevented by decreasing fatty-acid unsaturation as a common therapeutic approach.

Key words: **α-synuclein; cytosolic excess; fatty acid; membrane excess**

Significance Statement

α-Synuclein (αS) dyshomeostasis is linked to Parkinson's disease. Here we focus on two contrasting familial-Parkinson's disease αS mutants, E46K and G51D, that alter αS membrane association in opposite directions (E46K increases, G51D decreases it). Taking advantage of αS repeat structure, here we designed αS "3D," an amplified G51D variant (V40D+G51D+V66D). αS 3D further enhanced G51D's cytosolic enrichment. Systematic comparison of G51D/3D with membrane-enriched E46K/its amplified variant 3K revealed that both can elicit stress in human neural cells and primary rodent neurons. This toxicity can be ameliorated by inhibiting stearoyl-CoA desaturase or by saturated fatty acid conditioning. Thus, despite divergent membrane binding, both G51D and E46K αS dyshomeostasis are mitigated by altering fatty acid saturation as a shared target.

Introduction

Synucleinopathies, which include Parkinson disease (PD), dementia with Lewy bodies (DLBs), and multiple system atrophy (MSA), are a group of progressive, debilitating neurodegenerative diseases associated with α-synuclein (αS) aggregation in Lewy bodies and Lewy neurites, pathologic features cardinal to these diseases. PD affects >1% of the world population over the age of 60, making it the second most prevalent neurodegenerative disease globally and the most common synucleinopathy (de Lau and Breteler, 2006; Mhyre et al., 2012). Discovered as the first PD-associated gene, *SNCA* duplications/triplications (Singleton et al., 2003; Chartier-Harlin et al., 2004) and *SNCA* point mutations, namely, A53T (Polymeropoulos et al., 1997), A30P (Krüger et al., 1998), E46K (Zarranz et al., 2004), G51D (Kiely et al., 2013; Lesage et al., 2013), H50Q (Proukakis et al.,

Received Sep. 16, 2021; revised Jan. 6, 2022; accepted Jan. 13, 2022.

Author contributions: A.T., L.L., N.R., D.S., and U.D. designed research; A.T., H.A., E.T.-K., L.L., N.R., and U.D. performed research; A.T., A.N., L.L., T.I., S.F., S.N., N.R., D.S., and U.D. contributed unpublished reagents/analytic tools; A.T., H.A., E.T.-K., D.S., and U.D. analyzed data; A.T., D.S., and U.D. wrote the first draft of the paper; A.T., H.A., E.T.-K., A.N., L.L., T.I., S.F., S.N., N.R., D.S., and U.D. edited the paper; A.T., D.S., and U.D. wrote the paper.

This work was supported by National Institutes of Health Grants NS121826 and NS099328 to U.D., Grant NS083845 to D.S., and Grant NS109510 to S.N.; and the Michael J. Fox Foundation to S.F. The funders had no role in study design, data collection and analysis, decision to publish, or preparation of the manuscript. We thank Vikram Khurana (BWH/HMS), Matt LaVoie (University of Florida), and Tim Bartels (University College London) for helpful discussions; and Lai Ding and the NeuroTechnology Studio at BWH for providing access to the Incucyte machine and consultation on data acquisition.

D.S. is a director and consultant to Prothena Biosciences. The remaining authors declare no competing financial interests.

Correspondence should be addressed to Arati Tripathi at atripathi3@bwh.harvard.edu or Ulf Dettmer at udettmer@bwh.harvard.edu.

https://doi.org/10.1523/JNEUROSCI.1881-21.2022

2013), A53E (Pasanen et al., 2014), and A30G (Liu et al., 2021), have each been identified as causing forms of autosomal dominant "familial" PD (fPD). Certain missense mutations, such as E46K and G51D, display partially different clinical and neuropathological features. For E46K patients, these include severe parkinsonism as well as DLB (Zarranz et al., 2004). Patients bearing a G51D allele exhibit PD with dementia while the sole neuropathological report also revealed glial cytoplasmic inclusions in oligodendrocytes reminiscent of MSA (Kiely et al., 2013), suggesting a PD/DLB/MSA spectrum. The variability in clinical presentation and neuropathology between E46K and G51D is expected to be a consequence of their underlying biochemical mechanisms, which are not yet understood.

Several studies have examined the rate of αS aggregation or fibril formation *in vitro*, with E46K accelerating and G51D slowing oligomerization propensity versus WT αS (Pandey et al., 2006; Lesage et al., 2013; Fares et al., 2014; Flagmeier et al., 2016). αS can occur as a soluble unfolded protein *in vitro* (Weinreb et al., 1996; Bertoncini et al., 2007) and when overexpressed in protein-transfected cells (Binolfi et al., 2012; Theillet et al., 2016). It also associates with membranes (Kahle et al., 2000; Fortin et al., 2010; Ramalingam and Dettmer, 2021) and can attain a helically folded state on membrane interaction *in vitro* (Davidson et al., 1998; Chandra et al., 2003; Jao et al., 2004, 2008). In addition, aggregation-resistant helical tetrameric/multimeric assemblies have been described (Bartels et al., 2011; Wang et al., 2011) that are partially destabilized by fPD-causing αS missense mutations (Dettmer et al., 2015) as well as by loss-of-function mutations in glucocerebrosidase (*GBA*), a major PD risk factor (Kim et al., 2018). A deeper understanding of how the partitioning of αS between different assembly forms and membrane-bound versus aqueously soluble states can alter cellular homeostasis should inform us about underlying pathogenic mechanisms and guide therapeutic development. With these goals in mind, and taking advantage of the canonical 11-residue repeat structure, we developed a protein-engineering-based approach to selectively populate certain αS states in cultured cells. E46K shows increased phospholipid membrane binding compared with WT αS (Choi et al., 2004; Zarranz et al., 2004; Perlmutter et al., 2009; Rovere et al., 2019). In order to enhance this effect, we previously engineered the "3K" mutant by inserting analogous E-to-K mutations into the KTKEGV repeat motifs immediately adjacent to E46K (E35K+E46K+E61K) (Dettmer et al., 2015). The positive charges of 3K increase binding to negatively charged phospholipid membranes (Dettmer et al., 2015), which induces cytotoxicity (Dettmer et al., 2015, 2017; Imberdis et al., 2019b; Terry-Kantor et al., 2020), leads to a reduced multimer:monomer ratio, and causes lipid/membrane-rich αS accumulation (Dettmer et al., 2017; Ericsson et al., 2021). The latter change is reminiscent of the recent recharacterization of Lewy bodies as rich in lipid vesicles and membrane fragments, in addition to αS accumulation (Shahmoradian et al., 2019).

αS 3K transgenic mice exhibit a progressive PD-like phenotype with robust tremor and gait deficits (partially rescued by L-DOPA), loss of dopaminergic neurons, and formation of αS-rich inclusions in neuron cell bodies and neurites (Nuber et al., 2018). Based in part on this striking PD-like phenotype, we have used the 3K mutation as a drug discovery tool in cellular screens and identified stearoyl-CoA desaturase (SCD) as a key lipid modulator (Imberdis et al., 2019b) whose inhibition ameliorates αS-mediated toxicity in yeast (Fanning et al., 2018; Vincent et al., 2018), neural cells (Fanning et al., 2018; Vincent et al., 2018; Imberdis et al., 2019b; Terry-Kantor et al., 2020; Nicholatos et al., 2021), and mouse brain (Nuber et al., 2021) by re-equilibrating fatty acid (FA) homeostasis. These experimental observations collectively make the 3K αS amplification model suitable for addressing underlying mechanisms in PD with respect to excess αS-membrane binding. In contrast to membrane-avid E46K/3K, G51D impairs membrane association (Fares et al., 2014; Ysselstein et al., 2015), thereby increasing the soluble, cytosolic state of αS. However, there is no consensus in the field on how G51D exerts its toxicity, which could in part be because of the subtle effects of G51D alone.

Here, we focus on the consequences of expressing the cytosol-enriched G51D mutation compared with the membrane-avid E46K mutant. We use a protein engineering method to design 3D αS (V40D+G51D+V66D) by inserting G51D-analogous mutations into the immediately adjacent 11-amino acid repeats (core motif: KTKEGV). We reasoned that this would bias αS even further toward a soluble state. We show in neural cells that 3D indeed is enriched in cytosol compared with G51D. Moreover, 3D further exacerbates the reduction in multimer (αS60) to monomer (αS14) ratio observed on expression of G51D in neural cells. 3D and 3K enhance the cellular effects of G51D and E46K, respectively, and elicit increased toxicity when expressed in primary neurons. Both mutants lead to reduced cell growth in neural cells. The cellular stress exhibited by both the cytosol-preferring 1D and 3D and the membrane-preferring 1K and 3K αS can be decreased by pharmacological inhibition of SCD in neural cells and primary neurons. Moreover, conditioning in palmitic acid (16:0) or myristic acid (14:0) rescues the growth defect elicited by 3D, as previously shown for 3K (Imberdis et al., 2019b). Inhibiting SCD also alters the increased lipid droplets (LDs) of cells expressing the 3D and 3K variants. We show that SCD inhibition benefits G51D-expressing neural cells by increasing the aggregation-resistant multimer relative to the monomer. Together, our results indicate that the cell stress and biochemical properties of fPD mutants G51D and E46K are enhanced by rational design of their amplified mutants 3D and 3K in cultured neural cells and primary neurons. Despite their disparate membrane-binding preferences, both G51D-like and E46K-like cytotoxicity can be mitigated by SCD inhibition, pointing to a common underlying mono-unsaturated fatty acid (MUFA) metabolic alteration and a common therapeutic approach.

Materials and Methods

cDNA cloning. Mutant variant constructs were designed using GeneArt Strings DNA Fragments (Invitrogen) and ligated into pcDNA4/TO/myc-His and pLVX-TetOne-Puro lentiviral plasmid (Clontech/TaKaRa) plasmids using the In-Fusion HD cloning system (Takara) according to the manufacturer's instructions. αS variants were cloned into the pLVX-mCherry vector by restriction-enzyme-based cloning using SpeI/NotI sites.

Primary rat neuron harvest. Primary embryonic neurons were isolated from E18 Sprague Dawley rats. Dissected cortices were collected in HBSS on ice and digested with trypsin/EDTA at 37°C for 15 min followed by gentle trituration with a fire-polished Pasteur pipette in Neurobasal medium (Invitrogen) supplemented with B27, GlutaMAX (Invitrogen), penicillin (100 IU/ml), and streptomycin (100 μg/ml). Cells were then filtered through a 70 μm cell strainer (to remove tissue debris and clumps) and seeded in flat-bottom laminin/poly-L-ornithine-coated polystyrene plates (Corning, 354659) at a density of 50,000 cells (per well of 96-well plate) and 250,000 cells (per well of 24-well plate). The cells were cultured by keeping half the volume of existing supplemented Neurobasal medium in the wells and adding a fresh half of supplemented Neurobasal medium.

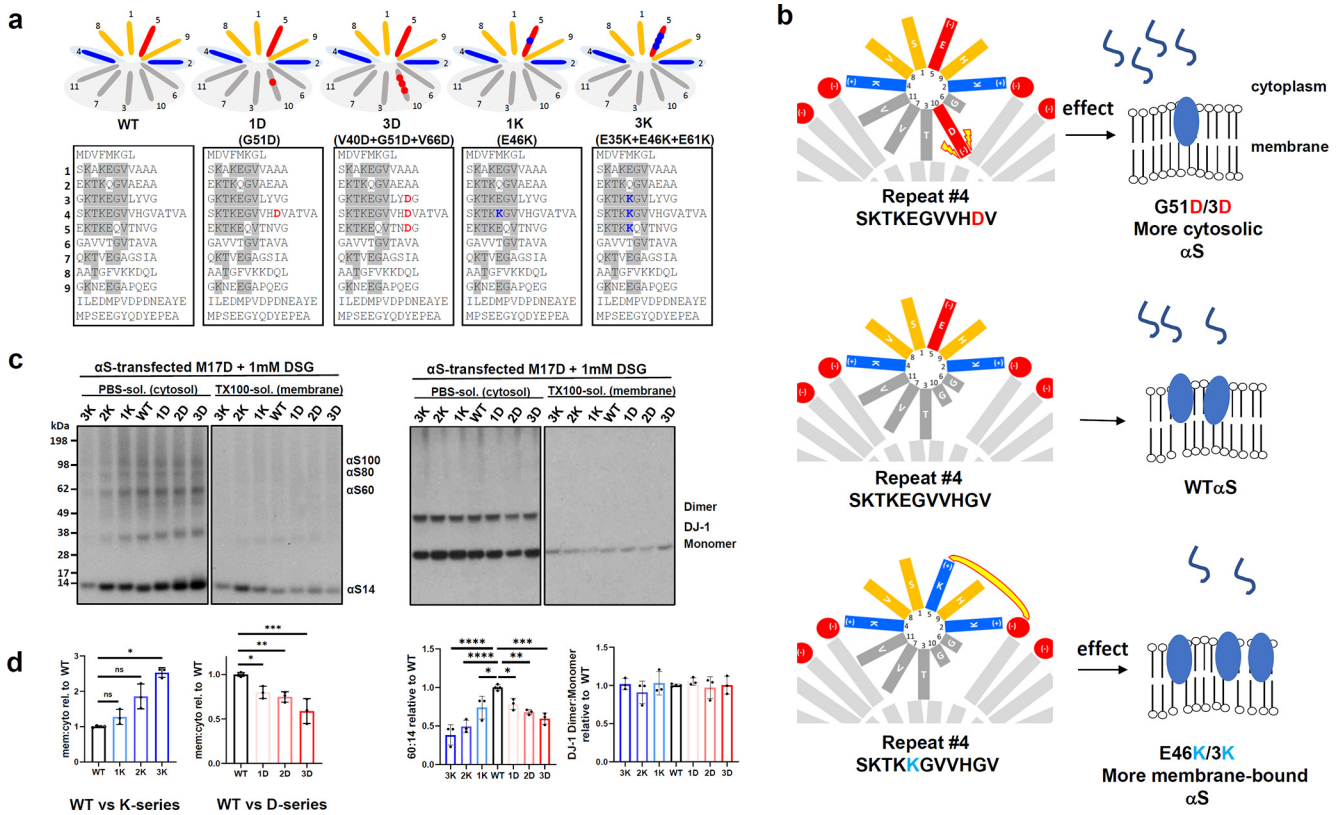

Figure 1. Strategically engineered αS variants 3D and 3K amplify biochemical effects of G51D (1D) and E46K (1K) in M17D neuroblastoma cells. ***a***, Helical wheel (11/3 helix) representation of a membrane-induced amphipathic helix of WT αS and 4 indicated variants. Blue represents basic aa. Red represents acidic aa. Gray represents αS region stabilized by hydrophobic interactions. Bottom, The αS variants aligned by the KTKEGV consensus motifs with residues that fully or partially conform to "KTKEGV" highlighted in gray. Red represents amino acid changes in G51D and 3D (V40D+G51D+V66D). Blue represents E46K and 3K (E35K+E46K+E61K). ***b***, Theoretical effects of E46K and G51D mutations on αS-membrane interactions. Positions of aa in repeat #4 (SKTKEGVVHGV) of membrane-embedded αS are shown. Red represents negatively charged lipid head groups. Pale gray represents FA tails. WT αS is stabilized by hydrophobic interactions (gray region) and electrostatic interactions (blue αS near red lipid head groups) as diagrammed in middle panel with folded αS (blue ovals, membrane) and unfolded monomers (curves, cytoplasm). G51D changes membrane-embedded residue G to negatively charged D creating repulsion (lightening arrows), leading to reduced membrane affinity and more cytosolic αS (top). E46K, on the other hand, changes membrane-proximal E to positive charge K (bottom), thereby leading to increased αS-membrane interactions (indicated by yellow curve) and more αS at the membrane. ***c***, M17D cells were transiently transfected with WT αS and indicated variants for 48 h. Intact-cell cross-linking with 1 mM DSG followed by sequential extraction of cytosolic and membrane proteins. WB for αS (mAb Syn1) and DJ-1 (control for cross-linking efficiency and protein loading). Variant 2D comprises mutations V40D+G51D and 2K comprises E35K+E46K. Representative WB of $N = 3$ independent experiments done on 3 different days. ***d***, Quantification of ***c***: αS cytosol:membrane and αS60:14 ratios and DJ-1 (control for cross-linking and loading); total $N = 3$ for all αS variants (WT was analyzed in duplicates in one experiment); WT (average) value was set to 1 in each independent experiment. *$p < 0.05$. **$p < 0.01$. ***$p < 0.001$. ****$p < 0.0001$. Additional accompanying data in Extended Data Figure 1-1.

Cell culture and transfection. Human BE(2)-M17 neuroblastoma cells (called M17D, ATCC #CRL-2267) and primary rat neurons were cultured at 37°C in 5% CO_2. M17D cells were cultured in DMEM supplemented with 10% FBS, penicillin (50 units/ml), streptomycin (50 µg/ml), and 1 mM L-glutamine for assays. Cells were transfected with Lipofectamine 2000 (Invitrogen) following the manufacturer's instructions.

Free FA loading. Free FAs used were myristic acid (Cayman, 13351), stearic acid (Cayman, 10011298), and oleic acid (Cayman, 90260). Cells were plated on d 1 using DMEM supplemented with 10% FBS and 1 mM glutamine. On d 2, media was removed and replaced with DMEM containing 2.5% FBS (starving condition); and 4 h after starvation, cells were treated with various concentrations of BSA/FA complexes. To prepare BSA/FA complexes, BSA was mixed with FAs in a ratio of 1:5 and incubated at 37°C for 30-60 min. Various concentrations of BSA/FA complex were added to cells for 3-4 h before adding doxycycline (1 mg/ml final concentration) to induce expression.

Intact-cell crosslinking. Transfected cells were collected by trituration, washed with PBS, and then resuspended in PBS with EDTA-free Complete Protease Inhibitor (Roche). Next, cells were crosslinked in 1 mM final concentration of disuccinimidyl glutarate (DSG) (Thermo Fisher Scientific) for 30 min at 37°C while rotating (Imberdis et al., 2019a). The reaction was then quenched by adding 50 mM Tris, pH 7.6, and incubating for 15 min at room temperature. Triton X-100 was then added at 1% final concentration and kept on ice for 10 min. Lysates were spun at 21,130 × *g* for 30 min. LDS sample buffer was added followed by boiling.

Total protein lysates and sequential protein extraction. Total protein lysates (cytosol and membrane) were generated by lysing cells in 1% Triton-X 100 detergent (Sigma) in PBS containing protease inhibitors. For sequential protein extraction, cells were resuspended in their media, transferred to 1.5 ml tubes, and centrifuged at 1500 × *g* for 5 min. Pellets were resuspended in 100 µl of dH_2O and incubated on a rotating wheel at 4°C for 5 min; 11 µl of 10× PBS was added, followed by ultracentrifugation at 100,000 × *g* for 30 min at 4°C. Supernatants were collected (cytosolic fraction), pellets were resuspended in 111 µl of 1× PBS 1% Triton X-100 and sonicated (Sonic Dismembrator model 300; microtip setting = 40; 15 pulses). Tubes were ultracentrifuged again, and supernatants were collected (membrane fraction). The resultant supernatant contained extracted membrane proteins.

Imaging-based assays. Calcein/propidium iodide (PI) assay (see Fig. 1*f*; Cayman 20 632/Invitrogen P3566) and WST assay (see Fig. 3*e*; Abcam ab155902) were performed following the manufacturers' instructions. Imaging-based toxicity assay "round versus flat" (see Fig. 2*a*,*b*), a total of 15,000 M17D cells per well (96-well plate), were plated on day 1. On day 2, each well was transfected with 100 ng DNA and Lipofectamine 2000 (Invitrogen; 11668030) following the manufacturer's instructions. Constructs used were

yellow fluorescent protein (YFP), αS-wt::YFP, αS-3D::YFP, and αS-3K::YFP. Cells were imaged and analyzed 38 h after transfection using the processing definition described by Terry-Kantor et al. (2020) to quantify green, round (dead) cells and green, flat (live) cells. The ratio of round to flat transfected cells was calculated relative to wt. Imaging-based toxicity assay "mCherry coexpression" (see Fig. 8): Rat primary neurons were transfected with pLVX-IRES-mCherry plasmids (αS wt, 1D, 3D, 1K, 3K); and 72 h after transfection we measured (1) total integrated area in the red channel (Incucyte standard processing definition) as a proxy for health of transfected cells, and (2) neurite length/cell body (Incucyte "Neurite Mask" processing definition) in the red channel as a proxy for neurite integrity. To measure the neurite length of rat cortical neurons, we used the Neurotrack processing definition in the IncuCyte Zoom 2016A software with the following parameters: cell body cluster parameter: top hat, radius (μm) 10, threshold (RCU) 2.0; cleanup: hole fill (μm^2) 0.0 – adjust size (pixels) 0 – minimum cell width (μm) 12.0; cell body cluster filters: area (μm^2), min 117.0. The following neurite parameters were used: neurite coarse sensitivity 9, neurite fine sensitivity 0.55; neurite width (μm) 1. Lipidspot 610 (#70069, Biotium) was added as per the manufacturer's instructions to detect LDs.

Immunoblotting. Samples were prepared for electrophoresis by lysis in the respective lysis buffer, addition of 4× NuPAGE LDS sample buffer, and boiling for 10 min. Samples were electrophoresed on NuPAGE 4%-12% Bis-Tris gels with NuPAGE MES-SDS running buffer and SeeBlue Plus2 molecular weight marker (all by Invitrogen) at 120 V and transferred in the iBlot 2 system (Invitrogen) to PVDF membranes (iBlot 2 PVDF regular stacks; IB401031). Membranes were fixed for 10 min in 4% PFA (in PBS). Membranes were blocked in blocking buffer (TBS blocking buffer, LiCor 927-60001) for 1 h and incubated in primary antibody in blocking buffer overnight at 4 °C. Membranes were washed 3 × 5 min in PBST or TBST. Secondary antibodies were prepared in the blocking buffer and incubated for 1 h at room temperature. Membranes were washed 3 × 10 min in PBST or TBST and scanned (Odyssey CLx, Li-Cor).

ELISA. Cell lysates from transfected cells were diluted with 1% BSA in wash buffer (TBS supplemented with 0.05% Tween). For total αS and pS129 αS assays, each well of an uncoated 96-well multiarray plate (Meso Scale Discovery, #L15XA-3) was coated with 30 μl of a PBS solution containing 3 μg/ml of MJFR1 (for total) or MJFR13 (for pS129) capture antibody (Abcam) and incubated at room temperature overnight. A detection antibody solution was prepared with biotinylated Syn1 antibody (BD Bioscience), plus 100 ng/ml Streptavidin Sulfo-TAG (Meso Scale Discovery, #R32AD-5) and 1% BSA diluted in wash buffer. Following overnight incubation, 50 μl/well of the sample plus 25 μl/well of the detection antibody solution were incubated for 2 h at room temperature with shaking at >300 rpm, washing wells with wash buffer between incubations. The plate was read and analyzed according to manufacturer's protocol.

Immunocytochemistry. Primary cortical neurons were fixed in 4% PFA in PBS for 10 min and washed 3 × 5 min in PBS. Cells were then permeabilized in PBS/1% Triton X-100 for 10 min and washed 3 × 5 min with PBS. First, antibodies were prepared in TBS/10% goat serum and incubated for 1 h at room temperature. Cells were washed 3 × 5 min in PBS and incubated for 1 h with secondary antibodies in TBS/10% goat serum. Nuclei were visualized by adding Hoechst dye (Invitrogen; H3570) at 1:2000 for 5 min. Cells were washed 3 × 5 min in PBS and imaged on InCell2200.

Antibodies. Primary antibodies used were monoclonal 15G7 [30] to αS (hybridoma supernatant; 1:500 in Western blot [WB]), monoclonal syn1 610786 (BD Biosciences; 1:1000 in WB), anti-DJ-1 (Baulac et al., 2004) (1:3000 in WB), mAb 6C5 to GAPDH (Santa Cruz Biotechnology; 1:1000 in WB), and polyclonal cleaved poly-adenosine 5′-diphosphate-ribose polymerase (PARP, Asp214) #9541S (Cell Signaling Technology, 1:1000 in WB). Secondary antibodies used were LiCor IRDye (926-68076, 926-32212, and 926-32211, 1:10,000 for WB).

Compounds. The SCD inhibitors used were CAY10566 (Abcam, ab144421) and MF-438 (Millipore Sigma, 569406).

Statistical analyses. We performed one-way ANOVA including Tukey's or Dunnett's or unpaired two-tailed *t* tests using GraphPad Prism version 9 following the program's guidelines. Normal distribution and similar variance were observed for all values. Values in graphs are mean ± SD. Criteria for significance were routinely determined relative to wt αS (shown in figures). Sufficient experiments and replicates were analyzed to achieve statistical significance and these judgments were based on earlier, similar work.

Results

Amplified E46K and G51D αS decrease cellular health in human neuroblastoma cells

Two missense mutations in αS, E46K and G51D, are each causative of autosomal dominant PD (Zarranz et al., 2004; Lesage et al., 2013; Kiely et al., 2015). The αS protein contains six to nine imperfect 11-residue repeats with the core consensus sequence KTKEGV (Maroteaux et al., 1988) and adopts a helical conformation on binding to lipid membranes (Davidson et al., 1998; Chandra et al., 2003; Jao et al., 2004, 2008). E46K changes the core sequence in repeat #4 from KTKEGV to KTKKGV, changing a negative to a positive charge in the helical region believed to be lying along the outside of vesicle membranes, whereas G51D introduces a negative charge in a hydrophobic stretch presumed to be embedded in the outer leaflet of the vesicle membrane (Fig. 1*a*,*b*). We reasoned that the nature of these disparate mutations should alter αS-membrane interactions in opposite directions (Fig. 1*b*), although both produce the clinicopathological syndrome of PD. E46K should increase αS-membrane association while G51D should decrease it and lead to increased cytosolic presence (Fig. 1*b*). Indeed, it has been reported that E46K stabilizes αS-membrane interactions, presumably via increased interaction with negatively charged lipid head groups (Choi et al., 2004; Perlmutter et al., 2009). This effect seems to be amplified by our engineered mutant 3K (E35K+E46K+E61K), generated by changing glutamate to lysine in repeats #3 and #5 analogous to clinical mutation E46K in repeat #4 (Fig. 1*a*) (Rovere et al., 2019). When expressed in human neuroblastoma cells, αS 3K causes cytotoxicity (Dettmer et al., 2015). When expressed as YFP-fusion proteins, αS E46K (1K) and to a much greater extent αS 3K form round cytoplasmic inclusions that can be studied longitudinally by live-cell microscopy (Imberdis et al., 2019b; Terry-Kantor et al., 2020). We predicted that, for the G51D mutation, in contrast, the reported reduction in membrane binding (Fares et al., 2014; Ysselstein et al., 2015) could be amplified by expressing the compound mutant 3D (V40D+G51D+V66D). This mutant was designed by changing valine (V) to aspartic acid (D) in repeats #3 and #5 at positions analogous to G51D in repeat #4 (Fig. 1*a*).

To test our hypothesis, we expressed αS WT, fPD mutants E46K (1K) and G51D (1D) as well as the compound mutants 2D (V40D+G51D), 3D, 2K (E35K+E46K), and 3K in M17D neuroblastoma cells that have low levels of endogenous αS (Dettmer et al., 2013). Intact-cell crosslinking followed by subcellular fractionation of the lysates into PBS-soluble (cytosol) and Triton X-100-soluble (membrane) fractions was performed (Imberdis et al., 2019a). Subsequent WB (equal loading) revealed that the fPD-linked αS mutations, 1D and 1K, both decreased the αS multimer:monomer (αS60:14) ratio, consistent with a previous report (Dettmer et al., 2015), and the 3D and 3K variants exacerbated these decreases (Fig. 1*d*, right). 3K expression led to further increase in αS membrane:cytosol ratio relative to 1K (Fig. 1*c*,*d*, left), demonstrating preference of 3K for membranes. This is in accord with a

previous characterization of αS 3K (Dettmer et al., 2015). In contrast, the 3D mutant decreased the αS membrane:cytosol ratio compared with 1D and 2D variants (Fig. 1*c*,*d*, left), demonstrating an increased cytosolic localization. To lend support to our observation that increased D substitutions led to a shift toward αS cytosol excess while K substitutions led to increased membrane preference, we expanded our list of engineered αS variants to include 4D (A29D+V40D+G51D+V66D), 6D (A18D+A29D+V40D+G51D+V66D+V88D), 4K (Q24K+E35K+E46K+E61K), and 6K (E13K+Q24K+E35K+E46K+E61K+E83K) mutants as part of the same experiment as in Figure 1*c*. We found that, while the levels of total PBS-soluble (cytosolic) αS were elevated in a stepwise fashion going from WT to 6D (Extended Fig. 1-1*a*,*b*, top left), there was no significant corresponding increase in the amount of membrane-associated αS. This strongly suggested that the distribution of αS toward the cytosol was independent of total αS levels and likely because of effects of the increasing D substitutions on αS. In contrast, a stepwise trend toward membrane association was seen for αS 1K-6K variants (Extended Fig. 1-1*a*,*b*, top right). Moreover, we will demonstrate below (see Fig. 3*a*) that, even with similar αS expression levels, 3D is more cytosolic than WT while 3K is more membrane-associated.

We chose 3D and 3K to further elucidate the consequences of expressing two opposite αS variants in a mildly exaggerated fashion. We reasoned that both 3D and 3K had the same number of alterations in the αS sequence and showed significant but opposite changes in their cellular distribution (3D cytosolic; 3K membrane). In addition, a mouse model of 3K αS has been shown to exhibit a robust PD phenotype (Nuber et al., 2018), further supporting a comparison of 3D versus 3K.

In order to assess the impact of 3D and 3K on αS distribution in live cells, we expressed these variants as YFP-fusion proteins in M17D neuroblastoma cells. The YFP signal was observed by live-cell fluorescence microscopy in the automated Incucyte time-lapse photography system (Fig. 2*a*). In accord with earlier reports (Dettmer et al., 2015, 2017; Ericsson et al., 2021), the 3K mutant exhibited a punctate inclusion phenotype in the cytoplasm consistent with its increased affinity for vesicle membranes and LDs (Fig. 2*a*, right; dotted arrows indicate inclusions). The appearance of αS seen on WT::YFP expression confirmed our previous results in M17D cells that showed WT diffusely in the cytoplasm (Dettmer et al., 2015). In 3D::YFP-expressing cells, localization of αS was indistinguishable from WT, indicating that 3D::YFP, like WT αS, is largely cytosolic (Fig. 2*a*, left vs middle). Together, these results suggested that, compared with the amplified mutant 3K, the amplified 3D mutant has far less membrane association and is cytosolically distributed.

Close inspection of the M17D transfectants revealed the frequent presence of cells with rounded morphology in both 3D::YFP and 3K::YFP cultures relative to WT::YFP cultures (Fig. 2*a*: white arrowheads indicate rounded cells; white solid arrows indicate flat cells). As an approximation for cellular health, we quantified the ratio of rounded (presumptively "stressed") cells to flat (presumptively unaffected) cells. This approach revealed that the 3K::YFP mutant significantly altered apparent cellular health (a mean 1.78 ± 0.29 increase of the rounded:flat cell ratio relative to WT::YFP) (Fig. 2*b*). 3D::YFP-expressing cells showed an intermediate reduction in health relative to WT::YFP (1.36 ± 0.15 mean increase of rounded:flat cell ratio relative to WT) (Fig. 2*b*). As an independent readout, we used the well-established calcein-AM and PI dye-based assay that stains live versus dead cells, respectively. We determined the ratio of the fluorescent signal for calcein-AM to protease inhibitor relative to WT::YFP-expressing cells. This analysis revealed a similar decrease in cell

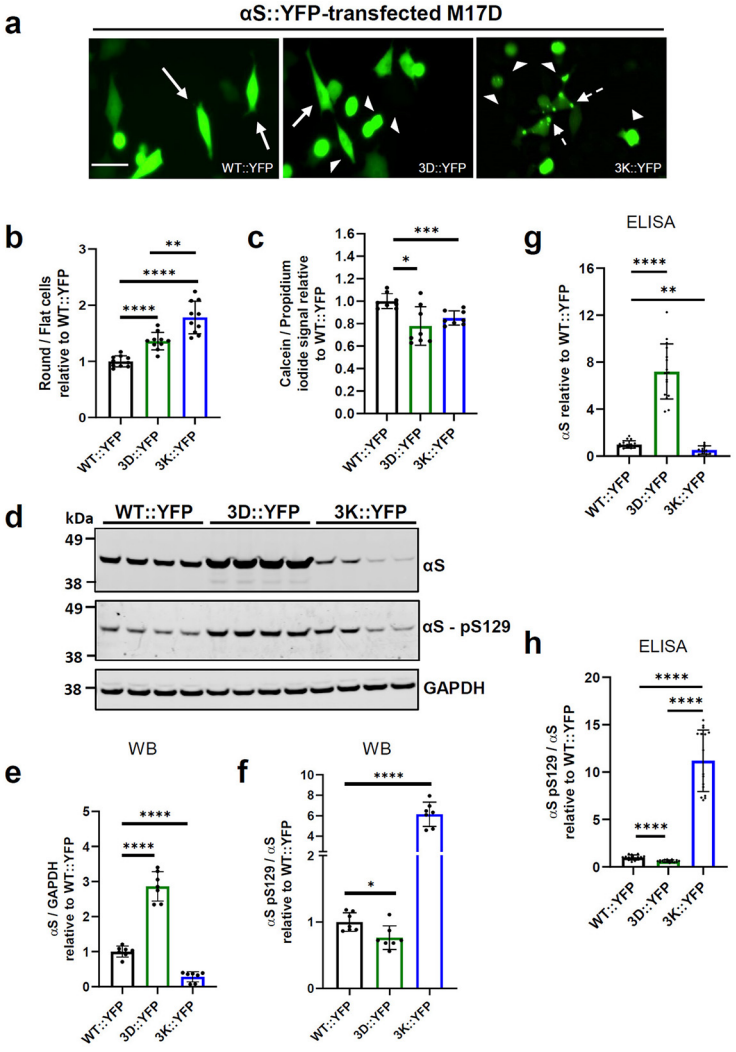

Figure 2. Engineered variants 3D and 3K elicit stress in M17D neural cells and alter αS levels. ***a***, Representative fluorescent microscopy images of αS WT and indicated variants fused to YFP and transiently expressed in M17D cells (38 h). Arrows indicate flat, healthy-looking cells. Arrowheads indicate rounded cells. Dotted arrows indicate cells bearing inclusions. Scale bar, 50 µm. ***b***, Quantification of transfected cells shown in ***a***: ratio of rounded to flat cells for all transfections relative to WT::YFP. Data represent $N = 3$ independent experiments with total $n = 10$. ***c***, Fluorescence signal ratio of calcein-AM total PI-stained cells relative to WT::YFP-expressing M17D cells. Graph represents total $n = 8$. ***d***, WB for αS-pS129, total αS (mAb 15G7), and GAPDH (loading control). ***e***, Quantification of total αS:GAPDH and (***f***) pS129:total αS ratios (normalized to WT::YFP); graph represents $N = 2$ independent experiments with total $n = 7$. ***g***, ELISA measurement of total αS and (***h***) pS129:total αS levels. Experimental setup as in ***a***. ELISA was performed on $N = 2$ independent days in 8 replicates each (total $n = 16$) for both ***g*** and ***h***. Data are mean ± SD. $^{*}p < 0.05$. $^{**}p < 0.01$. $^{***}p < 0.001$. $^{****}p < 0.0001$.

viability for both 3D::YFP and 3K::YFP mutants compared with WT::YFP-expressing M17D cells (Fig. 2*c*).

Levels of total αS and relative serine 129 phosphorylation are altered in 3D::YFP and 3K::YFP-expressing human neuroblastoma cells

We next subjected lysates of M17D cells expressing WT::YFP, 3D::YFP, and 3K::YFP to WB and measured the levels of total αS and serine 129 phosphorylated αS (αS-pS129) (Fig. 2*d*). Excess pS129 is widely accepted as a PD-relevant marker of αS abnormality (e.g., Zhou et al., 2011; Walker et al., 2013). Quantification revealed that total αS was elevated in 3D::YFP-expressing cells relative to WT::YFP (mean fold difference 2.86 ± 0.42) (Fig. 2*e*). In contrast, 3K-expressing cells showed a reduction in total αS levels (0.28 ± 0.14 relative to WT::YFP) (Fig. 2*e*). The ratio of pS129 to total αS was elevated in 3K (mean 6.15 ± 1.19-fold) and modestly reduced in 3D cells (mean 0.76 ± 0.17-fold) compared with cells expressing WT::YFP αS (Fig. 2*f*). Independent testing of this observation by ELISA revealed closely similar results (Fig. 2*g*,*h*). Total αS levels by ELISA were markedly increased in 3D::YFP transfectants relative to WT::YFP while they were modestly but significantly decreased in the 3K::YFP transfectants (Fig. 2*g*). Consistent with our WB analysis, the ratio of pS129 to total αS by ELISA also showed opposing trends: higher in 3K::YFP cells and lower in 3D::YFP cells compared with WT::YFP cells (Fig. 2*h*). Thus, the two methods agree on the changes seen for total αS levels and the ratio of pS129 to total αS.

Inducible expression of αS 3D and 3K affects the health of human neuroblastoma lines

To assess the effects of αS variants in a homogeneous, regulated, and visualizable system, we generated human M17D neural cells that inducibly express YFP-tagged αS in the presence of doxycycline (Dox). This system allowed for precisely timed control of αS expression, while the YFP-tag enabled visualization of αS distribution in living cells. We first sought to establish the relationship between the WT::YFP, 1D::YFP, and 3D::YFP variants having matched total αS expression levels. We performed subcellular fractionation of lysates of the three Dox-inducible cell lines and analyzed the PBS-soluble cytosolic and Triton X-100-solubilized membrane fractions (Extended Data Fig. 3-1*a*). Compared with WT, the 1D variant increased the relative amount of αS in the soluble fraction consistent with our earlier observation (Fig. 1*c*,*d*) and previous reports of impaired membrane association (Fares et al., 2014). The 3D variant further enhanced this effect (Extended Data Fig. 3-1*a*). These observations, together with the data shown in Figure 1*c*, *d*, demonstrated that, regardless of the total αS expression level, the D substitutions (1D, 3D) lead to an increased cytosolic preference of αS. We have previously shown that αS 3K exacerbates the inclusion formation and cytotoxicity elicited by 1K in M17D cells (Dettmer et al., 2015). Given our observation in M17D cells that 3D amplifies the effect of 1D (Fig. 1*d*; Extended Data Fig. 3-1*a*), we compared and contrasted the two amplified mutants 3D and 3K in our dox-inducible M17D model. We started by characterizing the distribution of 3D::YFP and 3K::YFP αS variants by live-cell imaging (Extended Data Fig. 3-1*b*) and biochemical subcellular fractionation (Fig. 3*a*). Image analysis showed that 3D distribution was akin to WT while 3K again exhibited multiple punctate inclusions (Extended Data Fig. 3-1*b*), consistent with what we had observed for the transiently transfected M17D cells (Fig. 2*a*). Subcellular fractionation of lysates from all three cell lines showed that, compared with WT, 3D enhanced the soluble fraction of αS while 3K caused an increase in the membrane fraction (Fig. 3*a*). These results indicated that 3D and 3K variants alter the distribution of αS in opposite directions regardless of absence or presence of a YFP tag.

To investigate the consequences of expressing cytosol-enriched (3D) versus membrane-enriched (3K) αS on cell viability, we next characterized the inducible lines in a cell growth assay. Cells were plated at a low density in 96-well plates and allowed to adhere for 24 h. Expression of WT::YFP, 3D::YFP, or 3K::YFP was then induced by Dox, and cell growth was monitored over time. Cell confluence was quantified for induced (+Dox) cells relative to the uninduced (-Dox) condition for each individual line. WT::YFP induction produced no significant effects on cell growth over the course of 96 h (Fig. 3*b*, bottom, four black bars). In contrast, induced expression of 3D::YFP and 3K::YFP αS each led to pronounced effects on cell growth (Fig. 3*b*, middle four green bars and top four blue bars, respectively). The growth defects appeared as early as 48 h after induction, with the difference becoming most apparent at 96 h (Fig. 3*b*). Image analyses at the 96 h time point again illustrated that induction of WT::YFP did not cause growth defects: the mean confluence relative to uninduced cells was 0.95 ± 0.08 (Fig. 3*c*,*d*). In contrast, 3K::YFP expression caused a marked reduction in cell confluence relative to uninduced cells (0.58 ± 0.09; Fig. 3*c*,*d*). 3D::YFP cells showed a less pronounced but still substantial growth defect (0.75 ± 0.10; Fig. 3*c*,*d*). All subsequent assays were therefore analyzed based on this 96 h time point.

We next applied the widely used WST-1 (2-(4-iodophenyl)-3-(4-nitrophenyl)−5-(2,4-disulfophenyl)-2H-tetrazolium, monosodium salt) assay, which measures activity of mitochondrial dehydrogenases to assess cell viability and proliferation. WST-1 reagent was added to both uninduced and induced cells, and the conversion of the tetrazolium salt to a colored formazan product was measured. Both 3K::YFP and 3D::YFP inducible cells had significantly reduced levels of formazan relative to uninduced cells (mean values 0.57 ± 0.17 for 3K and 0.84 ± 0.05 for 3D relative to uninduced cells) (Fig. 3*e*). No significant effect was observed for WT::YFP-expressing cells (+Dox) compared with control (-Dox) (Fig. 3*e*). Together, the two independent assays, image-based confluence analysis (Fig. 3*c*,*d*) and WST-1 assay (Fig. 3*e*), supported the interpretation that both 3D and 3K cells undergo significant stress when Dox-induced. We sought to confirm whether cell survival was impacted by using PI, a stain that only enters membrane-compromised dying or dead cells. Image analysis and quantification of red PI fluorescence (Fig. 4*a*,*b*) for all three cell lines relative to uninduced (-Dox) revealed a pronounced increase only for 3K::YFP cells (mean value 8.5 ± 2.01-fold, relative to -Dox condition). This result suggested that by the 96 h time point, the 3K cells had developed both a growth defect and cell death. To investigate the potential mechanism of cell death, we probed for PARP1 cleavage by WB. We quantified the fraction of cleaved PARP for each cell line relative to uninduced. Only 3K::YFP elicited a cleaved PARP response, with levels 3.2-fold higher than in uninduced cells (mean value 3.24 ± 0.63; Fig. 4*c*), implicating PARP's apoptotic role in 3K::YFP-induced toxicity. The absence of both PI+ staining and elevated cleaved PARP in the 3D::YFP cells suggested an alternative mechanism that limits cell growth.

We next examined levels of total αS, phospho-αS (pS129) and GAPDH (as a loading control) by WB of Dox-induced and uninduced cultures at the 96 h time point (Fig. 4*d*–*f*). No relevant

αS levels were observed in uninduced cells, as expected. WT::YFP, 3D::YFP, and 3K::YFP inducible cells expressed αS at similar levels when induced (Fig. 4*d*,*e*). 3K::YFP cells exhibited a markedly increased ratio of pS129 to total αS compared with 3D::YFP and WT::YFP cells (Fig. 4*f*). Comparison of 3D and WT expressing cells revealed no significant difference.

SCD inhibition rescues decreased cell health caused by induced expression of αS 3D or 3K

Lipids play a central role in many cellular pathways associated with PD pathogenesis, such as oxidative stress, endosomal-lysosomal pathway dysfunction, ER stress, and altered immune responses. Indeed, several genes involved in lipid metabolism have been identified in genome-wide association studies as risk factors for PD (Simón-Sánchez et al., 2009; Nalls et al., 2014). Lipidomic studies have also reported PD-related lipid alterations in both patient brains and plasma (Adibhatla and Hatcher, 2007). More recently, work by us and others identified SCD, the rate-limiting enzyme for the formation of MUFAs from saturated FAs (SFAs), as a therapeutic target for ameliorating αS cytotoxicity, thus connecting lipid metabolism directly to αS biology (Fanning et al., 2018; Vincent et al., 2018; Imberdis et al., 2019b). Taking advantage of our Incucyte cell confluence assay, we previously demonstrated that an SCD inhibitor, MF-438, can rescue the stunted growth of M17D cells caused by 3K::YFP expression (Terry-Kantor et al., 2020). SCD inhibition improved cell growth and prevented 3K::YFP-mediated cytotoxicity, including a decrease in αS inclusion burden and redistribution of the protein to its normal cytosolic pattern (Fanning et al., 2018; Terry-Kantor et al., 2020). While 3D::YFP-expressing cells do not yield the αS-rich inclusions observed in 3K::YFP cells (Fig. 2*a*; Extended Data Fig. 3-1*b*), we asked whether altering FA homeostasis by inhibiting SCD might also alleviate the slow growth phenotype observed in our experiments. We first treated the cells with MF-438 (1 μm) for 24 h before inducing expression of WT::YFP, 3D::YFP, or 3K::YFP with Dox. Cell confluence was quantified in the unbiased Incucyte imaging system at 96 h. For each cell line, the relative confluence of untreated and uninduced cells at this time point served as the control (Fig. 5*a*: 0 h, -Dox/-MF). In accord with Figure 3*d*, induction of 3K::YFP reduced cell confluence (Fig. 5*a*: compare 3K column, 96 h, -Dox/-MF and 96 h, +Dox/-MF). In agreement with our earlier report (Terry-Kantor et al., 2020), the confluence of 3K::YFP-expressing cells became similar to uninduced cells in the presence of MF-438 (Fig. 5*a*: compare 3K column, 96 h, +Dox/-MF and 96 h, +Dox/+MF). Induced expression of 3D::YFP also lowered cell confluence (Fig. 5*a*: compare 3D column, 96 h, -Dox/-MF and 96 h, +Dox/-MF), consistent with our earlier observation in Figure 3*d*. Treatment

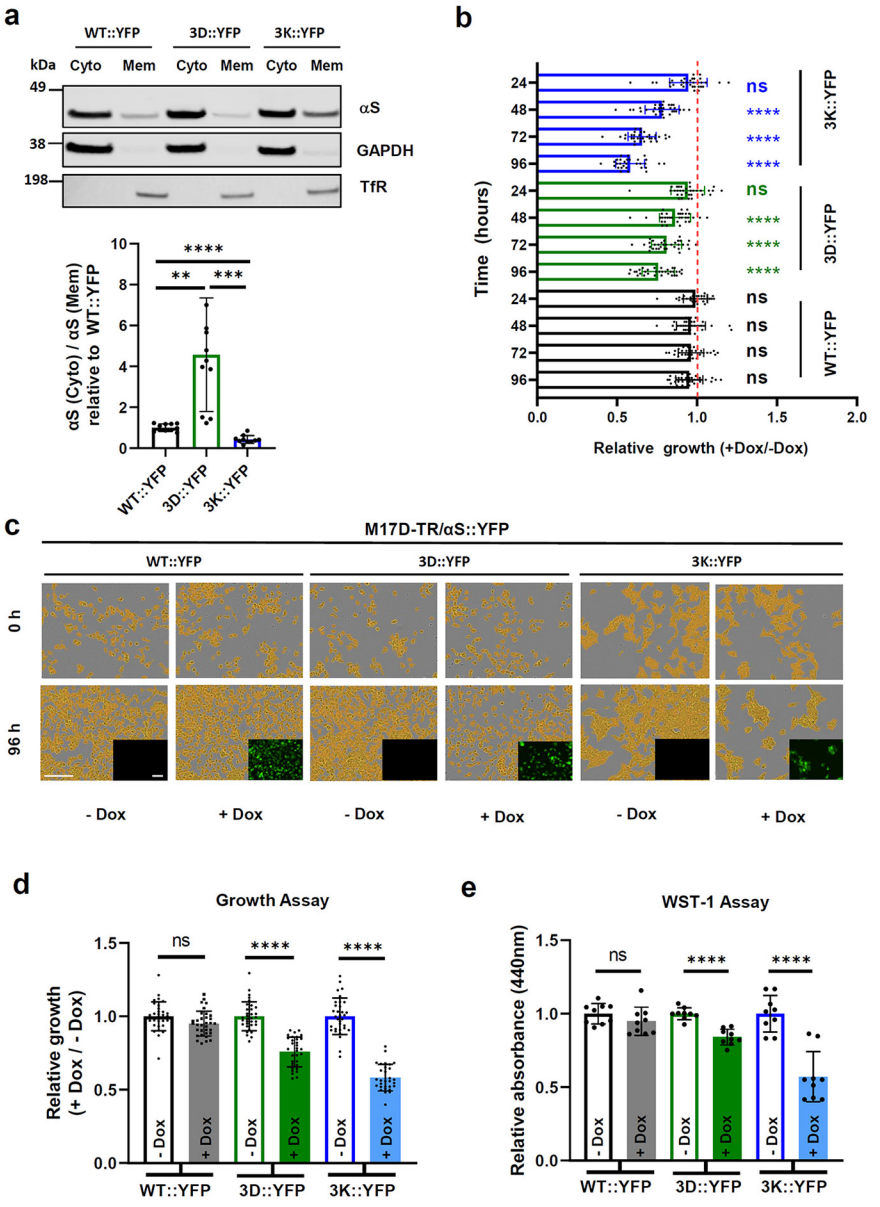

Figure 3. Induced expression of 3D and 3K elicits stress in M17D neural cells. ***a***, Sequential protein extraction αS WT::YFP, 3D::YFP, and 3K::YFP (induced for 48 h) into PBS (cyto) and Triton X-100 (mem) fractions. Top, WB total αS (mAb 15G7), GAPDH (cytosol marker), and transferrin receptor (TfR; membrane marker). Bottom, Quantitation of αS cyto versus mem relative to WT::YFP; $N = 3$ independent experiments, total $n = 10$ (WT::YFP, 3K::YFP) or $n = 8$ (3D::YFP cells). ***b***, αS::YFP was induced, and cell confluence was recorded after 0, 24, 48, 72, and 96 h by Incucyte. Quantitation relative to uninduced (+Dox/-Dox). As a baseline, red dashed line indicates normalized average fold growth of uninduced cells. $N = 7$ independent experiments, total $n = 33$. ***c***, Representative bright-field images recorded right before (0 h) and 96 h after addition of Dox (+Dox) or vehicle (-Dox). Orange represents cells identified by Incucyte. Bottom, Inset, YFP images 96 h after induction. Scale bar, 200 μm; inset, 100 μm. ***d***, Quantitation of ***c***, at 96 h after induction. Cell confluence defined as in ***c***, relative to uninduced (-Dox) condition for each cell line separately. Graph represents $N = 7$ independent experiments with total $n = 33$. ***e***, WST-1 assay to assess cell viability. WST-1 reagent added to -Dox and +Dox cells at 96 h, absorbance measured at 440 nm. Absorbance of +Dox relative to -Dox. $N = 3$ independent experiments, total $n = 9$. Data are mean ± SD. $^{**}p < 0.01$. $^{***}p < 0.001$. $^{****}p < 0.0001$. Additional accompanying data in Extended Data Figure 3-1.

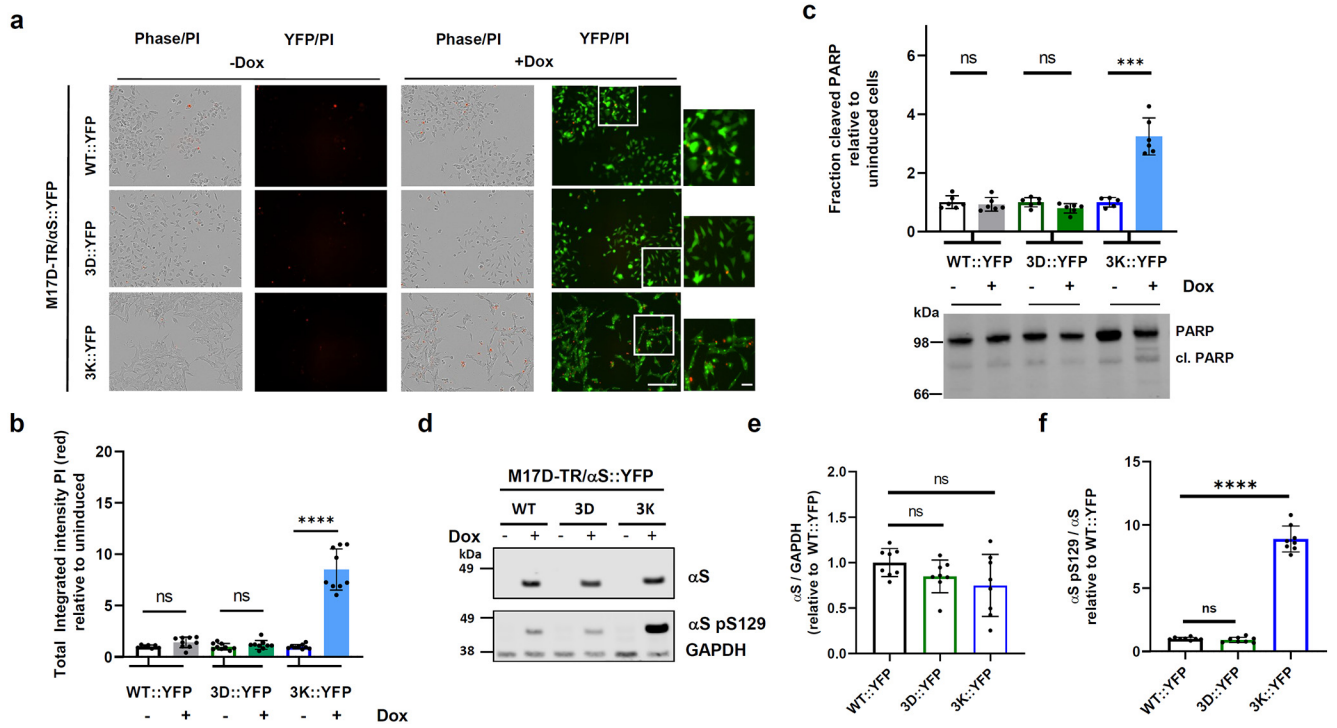

Figure 4. PI staining and PARP cleavage in αS::YFP inducible cell lines. ***a***, αS::YFP (WT, 3D, and 3K) was induced for 96 h. PI stain was added to -Dox and +Dox cells. Phase and YFP images were recorded for live cells by Incucyte. Scale bar, 250 μm; inset shows PI stain (red dots) along with YFP for induced cells. Scale bar, 50 μm. ***b***, Quantification of ***a***, as total integrated red PI intensity of +Dox relative to -Dox as indicated. $N = 3$ independent experiments with total $n = 9$ for all conditions, except total $n = 7$ for -Dox WT::YFP. ***c***, Expression of αS::YFP (WT, 3D, and 3K) was induced for 96 h. WB for PARP and cleaved PARP (cl. PARP). Bottom, WB. Top, Quantitation of cleaved PARP relative to -Dox as indicated. $N = 2$ independent experiments with total $n = 6$. ***d***, Expression of αS::YFP (WT, 3D, and 3K) was induced for 96 h, and levels of total αS (mAb 15G7), pS129, and GAPDH were assessed by WB. ***e***, Quantification of ***a***, αS:GAPDH ratios relative to WT::YFP cells. ***f***, Quantification of ***a***, pS129:total αS ratios relative to WT::YFP cells. $N = 2$ independent experiments with total $n = 8$ for both ***e*** and ***f***. Data are mean ± SD. $^{***}p < 0.001$. $^{****}p < 0.0001$.

with MF-438 rescued this growth defect of 3D::YFP-expressing cells (Fig. 5*a*: compare 96 h +Dox/-MF vs +Dox/+MF). Importantly, the compound neither elicited toxicity nor imparted benefit to any of the uninduced cell lines (Extended Data Fig. 5-1*a*: compare -Dox/-MF vs -Dox/+MF). We next quantified cell growth relative to the control condition (Fig. 5*b*: -Dox, open bar) for all three individual cell lines in the absence or presence of 1 μm MF-438. The SCD inhibitor minimally changed the mean confluence of WT::YFP cells from 0.92 ± 0.11 (Fig. 5*b*: +Dox, filled dark gray bar) to 1.08 ± 0.17 (Fig. 5*b*: +Dox+MF-438, filled pale gray bar). In contrast, the mean confluence of induced 3K::YFP cells improved from 0.65 ± 0.18 (Fig. 5*b*: +Dox, filled dark blue bar) to 0.90 ± 0.16 in the presence of MF-438 (Fig. 5*b*: +Dox+MF-438, filled pale blue bar), demonstrating rescue of the 3K::YFP-mediated growth defect. The stunted growth of 3D::YFP-expressing cells also benefitted from SCD inhibitor MF-438 and changed from 0.78 ± 0.12 (Fig. 5*b*: +Dox, dark green filled bar) in its absence to 1.02 ± 0.22 (Fig. 5*b*: +Dox+MF-438, light green filled bar) in the presence of MF-438. This result indicated that an SCD inhibitor can rescue the growth defect elicited by induced expression of 3D::YFP as well as 3K::YFP in human M17D neural cells.

Next, we compared in greater detail the YFP images of live cells in the presence or absence of MF-438 at 96 h after induction (Extended Data Fig. 5-1*b*). In 3K::YFP cells, αS+ inclusions observed in the +Dox condition appeared largely redistributed from round inclusions to a diffuse cytoplasmic localization (compare with +Dox/+MF-438 column, red box inset). There was no such effect in the 3D::YFP cells because this mutant produces no αS inclusions (Extended Data Fig. 5-1*b*). Similar to 3K::YFP-expressing cells, an increased number of YFP+ cells was observed in 3D::YFP cells treated with MF-438 (Extended Data Fig. 5-1*b*: compare +Dox and +Dox/+MF-438 columns), consistent with a mitigation of the cell growth defect.

SCD introduces a double bond in the *cis(-)*δ-9 position of several saturated fatty acyl-CoAs, including palmitoyl-CoA (16:0) and stearoyl-CoA (18:0), to yield the MUFAs palmitoleoyl- (16:1) and oleoyl-CoA (18:1), respectively. Apart from contributing to membrane phospholipids and sphingolipids, MUFAs are preferred substrates for the synthesis of triacylglycerols (TAGs) that can be mobilized into LDs. Recently, SCD inhibition was shown in 3K transgenic mice to decrease αS-mediated elevation of TAGs (Nuber et al., 2021). Therefore, we decided to test whether the rescue of growth defects in our inducible cells by SCD inhibition might correlate with changes in LDs. We analyzed lipid-staining patterns in live M17D cells expressing αS WT::YFP, 3D::YFP, or 3K::YFP, using a neutral lipid dye (LipidSpot; Biotium) and asked whether inhibiting SCD activity with MF-438 might alter LD biology. Compared with untreated cells, we observed a decrease in the size of LDs on treatment with MF-438, both in 3D- and 3K-expressing cells (Fig. 5*c*). Furthermore, the number of LDs in 3D cells treated with MF-438 was less than in untreated cells (Fig. 5*c*,*d*), resulting in a reduction of total integrated LD intensity (Fig. 5*c*, bottom left), which was absent for WT (Fig. 5*c*,*d*). These effects were consistent with studies in *Caenorhabditis elegans* showing that SCD deficiency results in fewer and smaller LDs (Shi et al., 2013). In contrast to these changes in 3D cells, MF-438 treatment of 3K

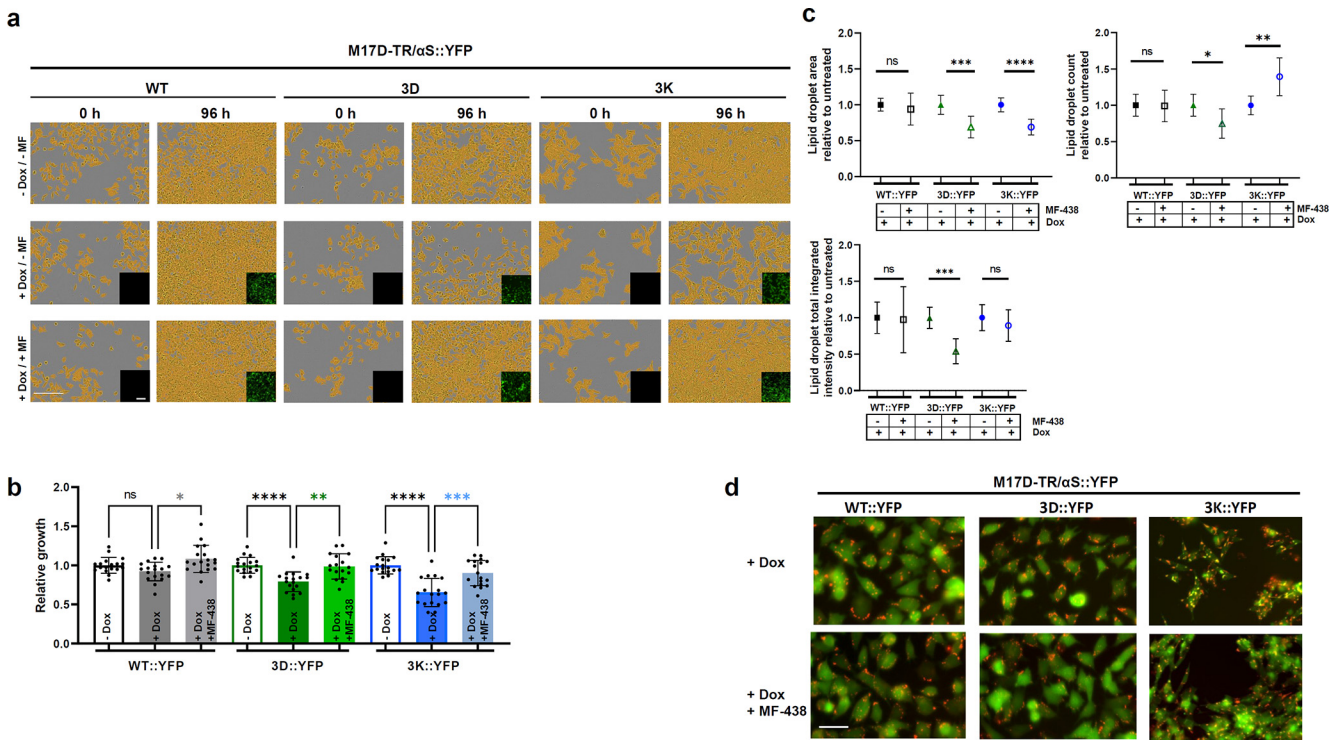

Figure 5. Stress exhibited by induced expression of engineered αS mutants 3D and 3K is ameliorated by pharmacological inhibition of SCD. ***a***, αS::YFP (WT, 3D, and 3K) cells treated with 1 μm SCD inhibitor MF-438 (+MF) or vehicle DMSO (-MF). Bright-field images at $t = 0$ h and $t = 96$ h, -Dox and +Dox. Orange represents cells identified by Incucyte. Inset, YFP images 96 h after Dox. TR, Tet-repressor element. Scale bar, 200 μm; inset, 100 μm. ***b***, Quantitation of ***a***, at 96 h after Dox. Growth quantitated analogous to Figure 3*c*, *d*. Cell confluence was measured relative to uninduced and untreated condition (-Dox/-MF) for each cell line separately. Graphs represent $N = 6$ independent experiments with total $n = 18$. ***c***, Quantitation of LD area, number, and intensity in the absence and presence of MF-438 relative to untreated induced cells (-MF-438/+Dox) for each of the indicated cell lines. LDs were stained with Lipidspot 610 (Biotium) dye 96 h after induction. Data are mean ± SD for $N = 3$ independent experiments with total $n = 9$ for all measurements. $^{*}p < 0.05$. $^{**}p < 0.01$. $^{***}p < 0.001$. $^{****}p < 0.0001$. ***d***, Representative live-cell images of WT::YFP, 3D::YFP, and 3K::YFP inducible cell lines treated with MF-438 (+Dox + MF-438) or untreated (+Dox), 96 h after induction, stained with Lipidspot 610 (red). TR, Tet-repressor element. Scale bar, 50 μm. Additional accompanying data in Extended Data Figure 5-1.

cells increased their LD number (Fig. 5*c*, top right) but decreased their size (Fig. 5*c*, top left), resulting in no overall change in total integrated LD intensity compared with untreated cells (Fig. 5*c*, bottom left). A decrease in LD size was similarly seen with the treatment of 3K-mice with an SCD inhibitor (Nuber et al., 2021). Together, these data suggested that inhibition of SCD activity influences LD size similarly in 3D and 3K αS cells but affects LD number differently.

Next, we performed quantitative WB of total αS in cell lysates of WT::YFP, 3D::YFP, and 3K::YFP inducible cells, with or without MF-438 treatment (Fig. 6*a*,*b*). We observed reduced levels of total αS for both 3D::YFP and 3K::YFP cells exposed to MF-438 (Fig. 6*b*). No significant changes in pS129 to total αS ratio were seen in all three lines with MF-438 (Extended Data Fig. 6-1).We have previously shown that fPD-linked αS mutations, including G51D and E46K, can alter the physiological αS multimer:monomer (60:14) equilibrium (Fig. 1*d*) (Dettmer et al., 2015). For E46K, this equilibrium can be corrected by decreasing MUFAs via SCD inhibition (Fanning et al., 2018; Imberdis et al., 2019b). To ascertain whether this holds true for fPD mutant G51D, human M17D neural cells stably expressing untagged G51D αS were treated with MF-438 (10 μM) for 48 h. Quantitative WB revealed an increase in the αS 60:14 ratio relative to untreated control cells on intact-cell DSG crosslinking (Fig. 6*c*). The endogenous DJ-1 dimer:monomer ratio was unchanged (Fig. 6*c*), serving as a negative control. The results suggested that elevating SFAs via SCD inhibition rescues αS imbalance caused by the clinical G51D PD-causing mutation.

Given that SCD plays an important role in converting SFAs to MUFAs, we hypothesized that SCD inhibition reduces dyshomeostasis by increasing the relative cellular concentration of SFAs in αS-expressing cells. In support of this idea, SFAs provided exogenously in the culture media had successfully rescued the inclusion phenotype observed in the 3K::YFP inducible cell line in a previous study (Imberdis et al., 2019b), thereby restoring cellular αS homeostasis. We therefore adapted this strategy for WT::YFP- and 3D::YFP-expressing cells. Since neither mutant formed inclusions reminiscent of 3K αS, we took advantage of our growth assay as a readout. M17D cells expressing WT::YFP or 3D::YFP αS were conditioned in the SFAs myristic acid (C14:0) or palmitic acid (C16:0) or the MUFA oleic acid (C18:1), and αS expression was induced after 4 h. Following 72 h conditioning, both SFAs (C14:0, C16:0) rescued the growth defect elicited by 3D αS, while no significant effect on growth of WT::YFP cells was seen under our assay conditions (Fig. 7*a*). Oleic acid (18:1) did not significantly alter the growth for either WT::YFP- or 3D::YFP-expressing cells (Fig. 7*b*). Our results lent support to the notion that augmenting SFA by FA loading mitigates αS-3D-related cellular stress.

Inclusion formation of αS 3K, but not 3D or WT αS in rat cortical neurons

Significant cytopathology of cortical neurons has been reported in PD patients, including those carrying G51D (Braak et al., 2003; Dickson, 2012; Lesage et al., 2013; Kiely et al., 2015). We therefore investigated the distribution of YFP-tagged WT, 3D,

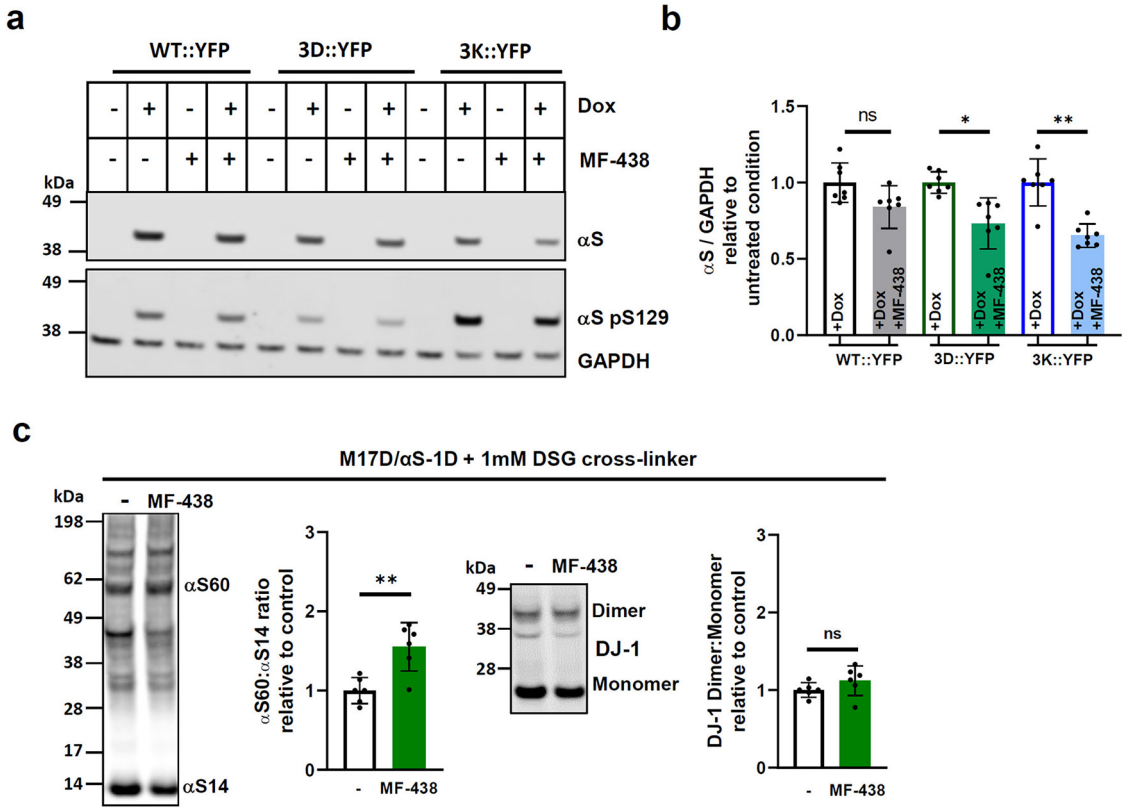

Figure 6. Biochemical effect of pharmacological inhibition of SCD. ***a***, WB of samples of Figure 5*b* for total αS (mAb 15G7), αS-pS129, and GAPDH. ***b***, Quantitation of ***a***, αS:GAPDH ratio in the absence and presence of SCD inhibitor MF-438; quantitation relative to induced cultures for each cell line as indicated 96 h after induction. $N = 3$ independent experiments with total $n = 7$. ***c***, M17D cells constitutively expressing untagged αS variant G51D were treated with 10 μM MF-438 or vehicle DMSO, and intact cell cross-linking (1 mM DSG) was performed. WB for total αS (mAb Syn1) and DJ-1 (control for equal cross-linking and loading). Quantification of αS60:αS14 and DJ-1 dimer:monomer ratios (normalized to untreated; $N = 4$ independent experiments with total $n = 6$). Data are mean ± SD. $^*p < 0.05$. $^{**}p < 0.01$. Additional accompanying data in Extended Data Figure 6-1.

and 3K αS in primary neurons from rat cortex. Rat cortical neurons were cotransfected with a plasmid expressing mCherry that served as a marker for the soluble phase of the cytoplasm, along with αS WT::YFP or its variants 3D::YFP and 3K::YFP. Similar to our observations in the human neuroblastoma cells, 3K::YFP-expressing neurons exhibited αS-positive inclusions (Extended Data Fig. 8-1; dotted arrow indicates an inclusion-rich neuron). In contrast, the 3D::YFP signal was diffuse throughout the soma and neurites, similar to that seen for mCherry distribution (Extended Data Fig. 8-1). WT::YFP was also distributed diffusely similar to mCherry, consistent with our previous work (Dettmer et al., 2015). We also noticed a decrease in number of neurites in both 3D::YFP and 3K::YFP neurons compared with WT::YFP (Extended Data Fig. 8-1), and we explored this phenotype further by expressing untagged αS in rat primary neurons (see below, Fig. 8). Our data thus far indicated that 3K expression in primary cortical neurons elicits an inclusion phenotype, whereas 3D appears cytosolic similar to WT-expressing neurons. Yet, both 3D and 3K may exhibit cytotoxicity in this model, as suggested by a visible loss of neurites.

Amplified E46K and G51D αS mutants affect neurite outgrowth in rat cortical neurons

Given that fPD mutants G51D (1D) and E46K (1K) exhibit cortical cytopathology in patients (Zarranz et al., 2004; Kiely et al., 2013), we chose to express untagged WT αS and variants 3D and 3K as well as the clinical mutations 1D and 1K in primary cortical neurons of normal rat embryos. The neurons were transiently transfected at 4 d *in vitro* with a bicistronic plasmid expressing mCherry and untagged human αS separated by an internal ribosomal entry site. The mCherry protein served as a filler, enabling clear visualization of the soma and neurites, enabling us to investigate the consequences of expressing untagged αS in neurons identified by mCherry. First, we examined the cellular distribution of αS 36 h after transfection by immunofluorescence imaging with the 15G7 antibody to human αS (Kahle et al., 2000) that does not recognize rat αS. Human WT αS and the variants 1D, 3D, and 1K, but not 3K, distributed throughout the soma and neurites (Fig. 8*a*). Cytosolic distribution of 1D was consistent with immunohistochemistry of G51D patient brain (Kiely et al., 2013). These results indicated that 3D and 3K alter the distribution of αS in opposite directions regardless of absence or presence of a YFP tag.

Next, we visualized the mCherry signal by live-cell fluorescence microscopy using the unbiased, automated Incucyte imaging system and quantified the red signal intensity as a proxy for cellular health at 72 h after transfection. 3K-expressing cortical neurons showed a pronounced decrease in mCherry intensity relative to WT (Fig. 8*c*: mean value 0.19 ± 0.04) consistent with previous reports (Dettmer et al., 2015, 2017). The 1K (mean value 0.81 ± 0.09) as well as 3D cells (mean value 0.72 ± 0.15) demonstrated intermediate levels, whereas 1D showed no significant changes versus WT (mean value 0.99 ± 0.25). We then asked whether this observed loss in fluorescence intensity correlated with a loss of neurite length. Quantification of neurite length per cell body revealed that 3D- and 3K-αS-expressing

neurons had modestly and markedly reduced neurite length, respectively (mean value vs WT 0.76 ± 0.06 and 0.30 ± 0.06, respectively), whereas 1D (mean value 0.92 ± 0.14) was not significantly shortened relative to WT (Fig. 8*b*, *d*). The decrease observed for 1K (mean value 0.77 ± 0.06 of WT) was exacerbated by the 3K mutant (mean value 0.31 ± 0.06 of WT). Our observations suggested that the amplifications of fPD mutants 1D and 1K, namely, to 3D and 3K based on the KTKEGV repeat structure, exacerbate the effects of the single point mutants in primary rat neurons. We next asked whether pharmacological inhibition of SCD would ameliorate the loss of neurite length in 3D-expressing neurons. In the presence of SCD inhibitor CAY10566 (CAY, Fig. 8*e*), the neurite length improved (mean value 1.48 ± 0.25 relative to untreated WT neurons) while untreated neurons had a significant loss of neurites (mean value 0.24 ± 0.15 for 3D vs untreated WT) 96 h after transfection.

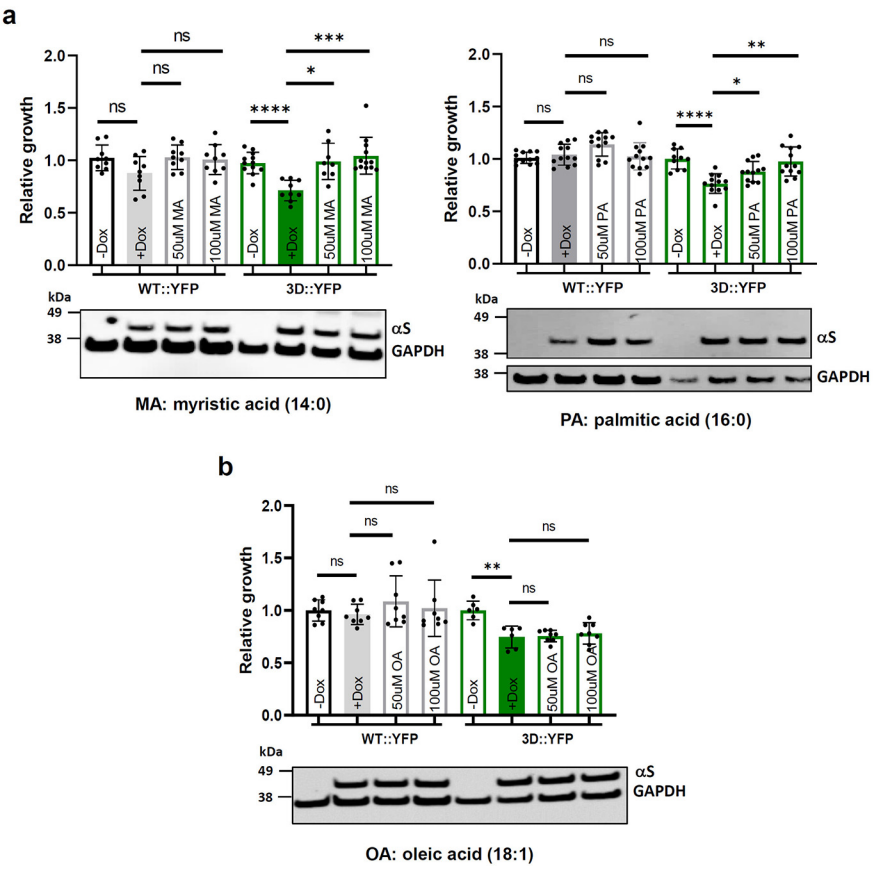

Figure 7. Effect of exogenous FAs on inducible cells expressing αS::YFP variants. WT::YFP and 3D::YFP inducible cell lines were treated with SFAs (***a***) C14:0 myristic acid (left) and C16:0 palmitic acid (right), or (***b***) MUFA C18:1 oleic acid (middle bottom) at indicated concentrations. Confluence of cells was quantitated as in Figure 3*c*, *d*, except at 72 h after induction. Bottom panel of each graph: representative WBs of total αS (mAb 15G7) and GAPDH. Data are mean ± SD for (***a***) 14:0 (myristic acid): $N = 3$ independent experiments, total $n = 9$ for all conditions except total $n = 12$ for 3D::YFP (-Dox column and 100 μM column); 16:0 (palmitic acid) $N = 3$, total $n = 12$ for all except total $n = 10$ for 3D::YFP (-Dox column); and (***b***) $N = 2$, total $n = 8$ for all except total $n = 6$ for 3D::YFP (-Dox and +Dox columns). *$p < 0.05$. **$p < 0.01$. ***$p < 0.001$. ****$p < 0.0001$.

Discussion

We have developed and continuously refined a protein engineering approach that takes advantage of the αS 11-mer repeat structure to selectively populate certain αS states in living cells (Dettmer, 2018). In previous work, we amplified the αS fPD mutant E46K to obtain αS 3K (E35K+E46K+E61K), which we have hypothesized to preferentially populate the monomeric, membrane-associated, amphipathic 3-11 helical conformation of αS (Dettmer et al., 2015). In the present work, we amplified instead the αS fPD mutant G51D to obtain αS 3D (V40D+G51D+V66D), which we hypothesize to preferentially populate the monomeric cytoplasmic unfolded conformation of αS. Consistent with these two hypotheses, we find αS 3K to be enriched as a 14 kDa monomer in the membrane (Triton X-100) fraction and αS 3D to be enriched as a 14 kDa monomer in the cytosol (PBS) fraction on intact-cell crosslinking and sequential extraction of transfected M17D human neuroblastoma cells (Fig. 1*c*,*d*, left). WT αS was found to be more cytoplasmic than 3K, more membrane-associated than 3D, and more multimer-forming than either of the variants (Fig. 1*c*,*d*). This observation is consistent with a model in which cytoplasmic αS multimer formation is a physiological event that is reduced under pathology-relevant conditions (here, fPD-causing αS mutations and their in-register amplification). Importantly, αS E46K and G51D alone exhibited the same trends as their respective amplifications, albeit less pronounced, as one might expect on structural grounds. We conclude that both 3K and 3D may be suitable for revealing disease-relevant features of the underlying fPD αS variants in an accelerated fashion, and we therefore performed a detailed comparative analysis.

Because it has been challenging for the PD field to achieve αS-related cytotoxicity by expressing WT or fPD single-mutant αS in the timescale of cell culture, we tested whether 3D might exhibit relevant stress on cells, as we had observed for 3K (Dettmer et al., 2015, 2017). Throughout the current study, there were several indications that expressing 3K and 3D each caused measurable cellular stress. Both amplified mutants increase the number of stressed cells on transient transfection of neuroblastoma cells (Fig. 2*a*–*c*). Both amplified variants reduced neurite length and viability of primary rat neurons (Fig. 8*c*,*d*). Both 3D and 3K reduced cellular growth in inducible neural cell lines (Fig. 3*d*). Our observation of rapid αS neurotoxicity caused by cytosol-accumulating variants like G51D and 3D seems at odds with findings in αS-expressing *Saccharomyces cerevisiae*: several studies observed that αS yeast toxicity is linked to increases in αS-membrane interaction while mutations that reduced membrane binding lower αS toxicity, even in the case of cytosol-accumulating fPD mutants, such as A30P or G51D (Volles and Lansbury, 2007; Fares et al., 2014; Newberry et al., 2020). Possible explanations for this apparent discrepancy could be that (1) cytosol-mediated αS toxicity requires the cellular context of higher organisms which express endogenous αS, in contrast to yeast; (2) cytosol-mediated αS toxicity is non–cell-autonomous; and/or (3) cytosol-mediated αS toxicity develops too slowly to be modeled appropriately in *Saccharomyces cerevisiae*. Our findings here with G51D and 3D are consistent with an earlier report that

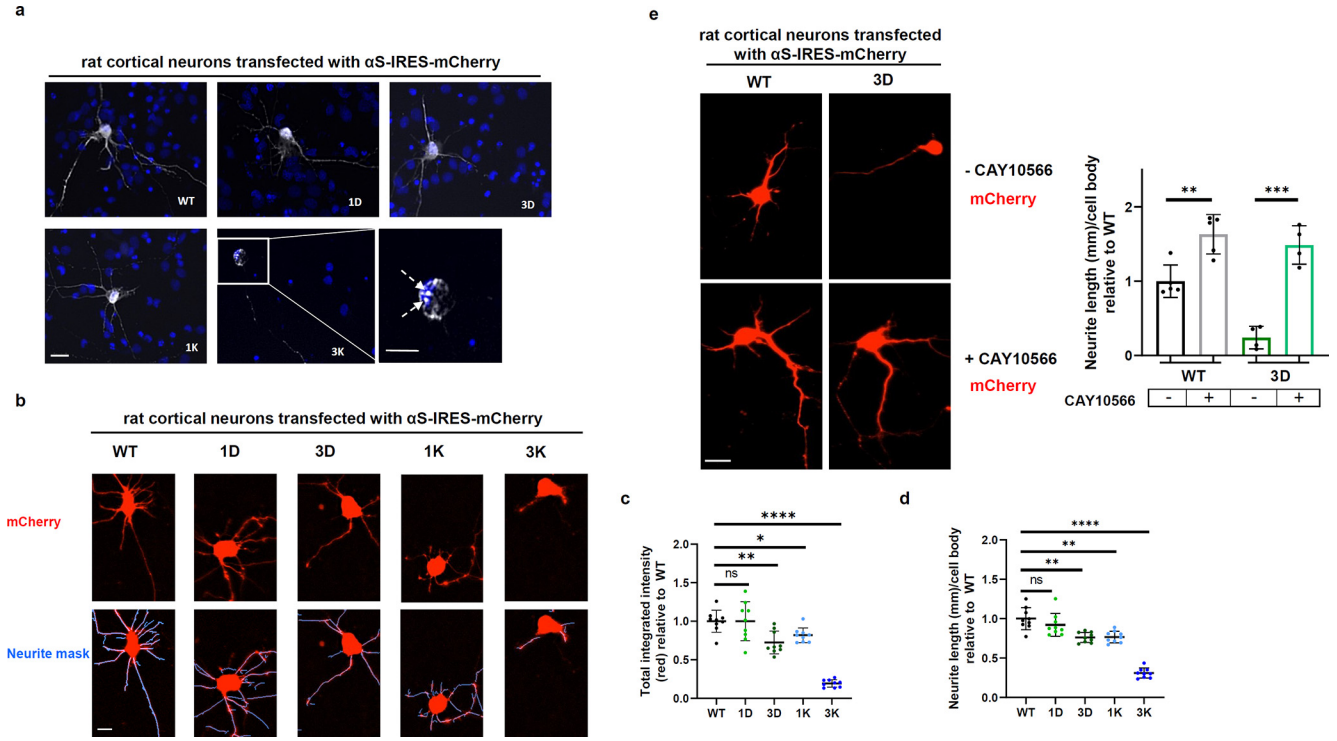

Figure 8. Amplified E46K and G51D αS mutants cause stress in primary rat cortical neurons. ***a***, Immunofluorescence images of primary rat cortical neurons transiently transfected with a bicistronic plasmid expressing mCherry and untagged human αS variants WT, 1D, 3D, 1K, and 3K (36 h after transfection); αS immunostaining (human-specific mAb 15G7) and Hoechst staining to visualize the nuclei. Scale bar, 200 μm; inset for 3K, 100 μm. ***b***, Fluorescence images of primary rat cortical neurons transiently transfected with a bicistronic plasmid expressing mCherry and untagged αS variants WT, 1D, 3D, 1K, and 3K (72 h after transfection). Top, mCherry distribution. Bottom, Neurite mask computed by Incucyte. Scale bar, 20 μm. ***c***, Comparison of total integrated intensity of mCherry signal computed with Incucyte system relative to that observed for αS WT. Same experimental setting as in ***b***, except analyzed at 72 h after transfection; graph represents $N = 3$ independent experiments with total $n = 9$. ***d***, Image-based analysis of neurite length as a measure of cellular stress. Quantitation of neurite length (mm/cell body) relative to αS WT expressing primary neurons computed using Incucyte. Experiment identical to ***c***; graph represents $N = 3$ independent experiments with total $n = 9$. ***e***, Image-based analysis of neurite length in the absence and presence of 50 nM SCD inhibitor CAY10566. Quantitation of neurite length (mm/cell body) relative to αS WT expressing primary neurons (CAY10566) computed using Incucyte; $n = 5$ (WT) and $n = 4$ (3D). Data are mean ± SD. *$p < 0.05$. **$p < 0.01$. ***$p < 0.001$. ****$p < 0.0001$. Additional accompanying data in Extended Data Figure 8-1.

reduced membrane association and consequently increased cytosolic preference by virtue of αS proline mutations can also exert toxicity in cultured human cells and rodents (Burré et al., 2015).

It is tempting to speculate that the G51D-like, cytosolic αS toxicity may be mediated by "classical" proteinaceous aggregation causing a proteinopathy: our data suggest that G51D, 2D, and 3D αS accumulate cytosolic monomeric αS in a "dose-dependent" fashion (Fig. 1*c*,*d*, left). Soluble monomeric αS has been suggested to be the starting point of αS aggregation (Bartels et al., 2011; Burré et al., 2015). However, we did not observe overt signs of YFP-tagged 1D or 3D aggregation in cultured cells the way it has been reported for preformed synthetic αS fibril-treated A53T::YFP-expressing HEK cells (Prusiner et al., 2015). WT::YFP, G51D::YFP, and 3D::YFP all seem to be uniformly distributed throughout the cytoplasm, and we observed no inclusion formation under our culture conditions, as we did with 3K (and E46K) (Fig. 2*a*; Extended Data Fig. 3-1*b*). Moreover, we found G51D and 3D aqueous solubility to be increased versus WT, not reduced as with E46K and 3K (Fig. 1*d*; Extended Data Fig. 3-1*a*), and intact-cell crosslinking revealed an increase in monomers but no crosslinked higher bands (e.g., increased dimers) that would suggest aggregate formation. Thus, any aggregates formed by the cytosolic-accumulating αS 1D/3D would be either low in abundance or not readily cross-linkable. αS G51D has been reported to exhibit nuclear localization and to be hyperphosphorylated (Fares et al., 2014). While we did not extensively test the former observation, our microscopy data do not seem to support substantial nuclear accumulation of 3D αS as an amplification of G51D. Regarding S129 phosphorylation, we observed either reduced phosphorylation levels or levels that were similar to WT αS, indicating that no hyperphosphorylation of G51D/3D occurs in our cultures. Under transient transfection, we observed elevated levels of G51D and even more of 3D (Fig. 1*c*,*d*, left), suggesting an altered half-life of these variants. However, the inducible 3D::YFP line, which exhibits pronounced growth defects relative to WT-expressing cells, had similar expression levels to WT.

αS monomers bind highly curved phospholipid membranes (Gitler et al., 2008; Burré et al., 2010; Nemani et al., 2010; Westphal and Chandra, 2013; Wang et al., 2014). E46K αS has a higher affinity for binding to negatively charged vesicles than WT (Choi et al., 2004), likely via abnormally increased membrane-induced amphipathic helix formation (Wise-Scira et al., 2013), and adding in-register E→K mutations into the two adjacent KTKEGV motifs in the N-terminal region (to generate the 3K αS mutant) further enhances this abnormality (Rovere et al., 2019). When the homeostatic balance of αS tetramer:monomer (60:14 ratio) is disrupted and excess αS monomers accumulate, abnormal αS+ vesicular/membrane-rich aggregates can form by virtue of its increased membrane affinity. Such membrane-rich aggregates (inclusions) have been observed in multiple model systems (Dettmer et al., 2015; Nuber et al., 2018; Imberdis et al., 2019b; Ericsson et al., 2021) and are reminiscent of the recently revised ultrastructure of Lewy bodies (Shahmoradian et al., 2019). Most importantly, we have reported a 3K αS transgenic (tg) mouse model where the physiological tetramer to monomer

ratio (αS 60:14 ratio) is decreased, and this correlated with resting tremor, gait changes, and other progressive motor deficits akin to those seen in PD subjects (Nuber et al., 2018). In both WT and 3K αS tg mice, prominent lipid elevations were found in glycerolipids (triglycerides) known to be regulated by SCD activity (Nuber et al., 2021). Similarly, in iPSC-neurons derived from an αS triplication patient, diglycerides and triglycerides were also notably increased (Fanning et al., 2018). Treatment of 3K αS tg mice with an SCD inhibitor decreased the 16:1/16:0 FA desaturation index and improved partitioning of αS monomers away from membranes toward principally cytosolic αS tetramers (i.e., improved the 60:14 ratio) (Nuber et al., 2021). These results collectively suggested that SCD treatment alleviates abnormal αS membrane–lipid interaction of excess WT or 3K αS monomers by creating a more αS-repellent membrane surface. In accord, less lipid-rich αS+ aggregates were observed on treatment with SCD inhibitor (Nuber et al., 2021).

Perhaps unexpectedly, based on the presumed opposing effects of the D and K mutants on αS-membrane interactions, we found evidence of altered lipid biology as a feature of 3D toxicity. Analogous to what we had seen for E46K and its amplification to 3K (Fanning et al., 2018; Imberdis et al., 2019b; Terry-Kantor et al., 2020), we found here that the αS dyshomeostasis and cellular stress caused by the strongly cytosol-preferring 3D mutant could be ameliorated by pharmacological inhibition of SCD, both in human neuroblastoma cells and primary rat cortical neurons (Figs. 5*b*, 8*e*). Further, we observed such amelioration by conditioning the 3D cells in palmitic acid (16:0) or myristic acid (14:0) (Fig. 7*a*). Moreover, both 3D and 3K αS expression was associated with alterations in LD content and/or morphology, which could be reversed in considerable part by SCD inhibition (Fig. 5*c*). We also observed that inhibition of SCD improved G51D αS homeostasis by increasing the ratio of tetramers/multimers to monomers (Fig. 6*c*). Molecular modeling suggests that the folded αS tetramer occupies the lowest apparent activation energy state among possible αS conformers (Cote et al., 2018; Xu et al., 2019), and it has been experimentally shown to resist aggregation (Bartels et al., 2011), suggesting that this energetically favored physiological state is likely protective for a cell. In addition to our present report (Fig. 1*c*,*d*, right), studies in multiple model systems, including human neural cells, human iPSc-derived neurons, and mouse models of synucleinopathy, indicate that fPD mutations reduce the αS 60:14 ratio (Dettmer et al., 2015; Fanning et al., 2018; Nuber et al., 2018, 2021; Imberdis et al., 2019b). The downshift in the ratio resulting from loss of incorporation of αS monomers into aggregation-resistant tetramers causes the accumulation of excess monomers in the cell. The excess monomers can aggregate in a way that appears similar in part to αS observed in Lewy bodies, classical neuropathological feature found in all PD patients, including E46K and G51D subjects. αS monomers, but not purified cellular tetramers, have also been shown to bend and stabilize vesicle membranes *in vitro* (Westphal and Chandra, 2013), which may in turn inhibit exocytic membrane fusion events at the synapse (Wang et al., 2014). In support, another report provided evidence for a physiological function of αS multimers (tetramers, octamers) in facilitating SNARE complex formation and vesicle fusion (Burré et al., 2014). Together, our present study and those mentioned above suggest that a reduced multimer:monomer ratio is associated with impaired cellular health, and restoring it benefits the cell. Our present findings highlight the cellular benefits of reestablishing normal tetramer/multimer to monomer balance by partially decreasing FA unsaturation via SCD inhibition.

While we do not yet fully understand the exact molecular mechanism by which "K" and "D" variants converge on FA metabolism, we hypothesize that αS monomers require a certain fatty acyl side chain composition on small-vesicle membranes to properly bind them, tetramerize, and then have the tetramers released from the membrane to enter the cytosol, where they are principally observed within cells. Our study is consistent with compelling evidence that alterations in lipid homeostasis can decrease αS60:αS14 ratios, as reported in human neurons bearing loss-of-function mutations in *GBA* that cause Gaucher's disease and PD (Kim et al., 2018). Using SCD inhibitors as done in our present study, or using genetic or pharmacological restoration of normal glucosylceramide levels as done in *GBA* models (Kim et al., 2018), correct the αS60:αS14 decrease, leading to improved cellular health. However, more work is needed to understand the precise nature of the FA/lipid changes that occur and are influenced by SCD treatment to benefit cellular health.

Together, our experiments suggest that, despite different charges and thus membrane binding affinities, the neurotoxicity of both G51D/3D and E46K/3K is mitigated by decreasing MUFA levels via SCD inhibition, suggesting a common underlying alteration of MUFA homeostasis. Our follow-up studies will dissect the interplay among free FAs, membrane fatty acyl side-chains, LDs, and αS (both D and K mutants and WT αS) variants, including detailed lipidomics of our cellular and emerging mouse models of G51D and 3D αS. Our future studies will also delve into potential accompanying changes in the transcriptome and proteome to gain insight.

References

Adibhatla RM, Hatcher JF (2007) Role of lipids in brain injury and diseases. Future Lipidol 2:403–422.

Bartels T, Choi JG, Selkoe DJ (2011) α-Synuclein occurs physiologically as a helically folded tetramer that resists aggregation. Nature 477:107–110.

Baulac S, LaVoie MJ, Strahle J, Schlossmacher MG, Xia W (2004) Dimerization of Parkinson's disease-causing DJ-1 and formation of high molecular weight complexes in human brain. Mol Cell Neurosci 27:236–246.

Bertoncini CW, Rasia RM, Lamberto GR, Binolfi A, Zweckstetter M, Griesinger C, Fernandez CO (2007) Structural characterization of the intrinsically unfolded protein beta-synuclein, a natural negative regulator of alpha-synuclein aggregation. J Mol Biol 372:708–722.

Binolfi A, Theillet FX, Selenko P (2012) Bacterial in-cell NMR of human α-synuclein: a disordered monomer by nature? Biochem Soc Trans 40:950–954.

Braak H, Del Tredici K, Rüb U, de Vos RA, Jansen Steur EN, Braak E (2003) Staging of brain pathology related to sporadic Parkinson's disease. Neurobiol Aging 24:197–211.

Burré J, Sharma M, Tsetsenis T, Buchman V, Etherton MR, Südhof TC (2010) Alpha-synuclein promotes SNARE-complex assembly in vivo and in vitro. Science 329:1663–1667.

Burré J, Sharma M, Sudhof TC (2014) alpha-Synuclein assembles into higher-order multimers upon membrane binding to promote SNARE complex formation. Proc Natl Acad Sci USA 111:E4274–E4283.

Burré J, Sharma M, Südhof TC (2015) Definition of a molecular pathway mediating α-synuclein neurotoxicity. J Neurosci 35:5221–5232.

Chandra S, Chen X, Rizo J, Jahn R, Südhof TC (2003) A broken alpha-helix in folded alpha-synuclein. J Biol Chem 278:15313–15318.

Chartier-Harlin MC, Kachergus J, Roumier C, Mouroux V, Douay X, Lincoln S, Levecque C, Larvor L, Andrieux J, Hulihan M, Waucquier N, Defebvre L, Amouyel P, Farrer M, Destée A (2004) Alpha-synuclein locus duplication as a cause of familial Parkinson's disease. Lancet 364:1167–1169.

Choi W, Zibaee S, Jakes R, Serpell LC, Davletov B, Crowther RA, Goedert M (2004) Mutation E46K increases phospholipid binding and assembly into filaments of human alpha-synuclein. FEBS Lett 576:363–368.

Cote Y, Delarue P, Scheraga HA, Senet P, Maisuradze GG (2018) From a highly disordered to a metastable state: uncovering insights of α-synuclein. ACS Chem Neurosci 9:1051–1065.

Davidson WS, Jonas A, Clayton DF, George JM (1998) Stabilization of alpha-synuclein secondary structure upon binding to synthetic membranes. J Biol Chem 273:9443–9449.

de Lau LM, Breteler MM (2006) Epidemiology of Parkinson's disease. Lancet Neurol 5:525–535.

Dettmer U (2018) Rationally designed variants of α-synuclein illuminate its in vivo structural properties in health and disease. Front Neurosci 12:623.

Dettmer U, Newman AJ, Luth ES, Bartels T, Selkoe D (2013) In vivo cross-linking reveals principally oligomeric forms of α-synuclein and β-synuclein in neurons and non-neural cells. J Biol Chem 288:6371–6385.

Dettmer U, Newman AJ, Soldner F, Luth ES, Kim NC, von Saucken VE, Sanderson JB, Jaenisch R, Bartels T, Selkoe D (2015) Parkinson-causing α-synuclein missense mutations shift native tetramers to monomers as a mechanism for disease initiation. Nat Commun 6:7314.

Dettmer U, Ramalingam N, von Saucken VE, Kim TE, Newman AJ, Terry-Kantor E, Nuber S, Ericsson M, Fanning S, Bartels T, Lindquist S, Levy OA, Selkoe D (2017) Loss of native α-synuclein multimerization by strategically mutating its amphipathic helix causes abnormal vesicle interactions in neuronal cells. Hum Mol Genet 26:3466–3481.

Dickson DW (2012) Parkinson's disease and parkinsonism: neuropathology. Cold Spring Harb Perspect Med 2:a009258.

Ericsson M, von Saucken V, Newman AJ, Doehr L, Hoesch C, Kim TE, Dettmer U (2021) Crowded organelles, lipid accumulation, and abnormal membrane tubulation in cellular models of enhanced α-synuclein membrane interaction. Brain Res 1758:147349.

Fanning S, Haque A, Imberdis T, Baru V, Inmaculada Barrasa M, Nuber S, Termine D, Ramalingam N, Ho GP, Noble T, Sandoe J, Lou Y, Landgraf D, Freyzon Y, Newby G, Soldner F, Terry-Kantor E, Kim TE, Hofbauer HF, Becuwe M, et al. (2018) Lipidomic analysis of α-synuclein neurotoxicity identifies stearoyl CoA desaturase as a target for Parkinson treatment. Mol Cell 73:1001–1014.e8.

Fares MB, Ait-Bouziad N, Dikiy I, Mbefo MK, Jovičić A, Kiely A, Holton JL, Lee SJ, Gitler AD, Eliezer D, Lashuel HA (2014) The novel Parkinson's disease linked mutation G51D attenuates in vitro aggregation and membrane binding of α-synuclein, and enhances its secretion and nuclear localization in cells. Hum Mol Genet 23:4491–4509.

Flagmeier P, Meisl G, Vendruscolo M, Knowles TP, Dobson CM, Buell AK, Galvagnion C (2016) Mutations associated with familial Parkinson's disease alter the initiation and amplification steps of α-synuclein aggregation. Proc Natl Acad Sci USA 113:10328–10333.

Fortin DL, Nemani VM, Nakamura K, Edwards RH (2010) The behavior of alpha-synuclein in neurons. Mov Disord 25 Suppl 1:S21–S26.

Gitler AD, Bevis BJ, Shorter J, Strathearn KE, Hamamichi S, Su LJ, Caldwell KA, Caldwell GA, Rochet JC, McCaffery JM, Barlowe C, Lindquist S (2008) The Parkinson's disease protein alpha-synuclein disrupts cellular Rab homeostasis. Proc Natl Acad Sci USA 105:145–150.

Imberdis T, Fanning S, Newman A, Ramalingam N, Dettmer U (2019a) Studying α-synuclein conformation by intact-cell cross-linking. Methods Mol Biol 1948:77–91.

Imberdis T, Negri J, Ramalingam N, Terry-Kantor E, Ho GP, Fanning S, Stirtz G, Kim TE, Levy OA, Young-Pearse TL, Selkoe D, Dettmer U (2019b) Cell models of lipid-rich α-synuclein aggregation validate known modifiers of α-synuclein biology and identify stearoyl-CoA desaturase. Proc Natl Acad Sci USA 116:20760–20769.

Jao CC, Der-Sarkissian A, Chen J, Langen R (2004) Structure of membrane-bound alpha-synuclein studied by site-directed spin labeling. Proc Natl Acad Sci USA 101:8331–8336.

Jao CC, Hegde BG, Chen J, Haworth IS, Langen R (2008) Structure of membrane-bound alpha-synuclein from site-directed spin labeling and computational refinement. Proc Natl Acad Sci USA 105:19666–19671.

Kahle PJ, Neumann M, Ozmen L, Muller V, Jacobsen H, Schindzielorz A, Okochi M, Leimer U, van Der Putten H, Probst A, Kremmer E, Kretzschmar HA, Haass C (2000) Subcellular localization of wild-type and Parkinson's disease-associated mutant alpha-synuclein in human and transgenic mouse brain. J Neurosci 20:6365–6373.

Kiely AP, Asi YT, Kara E, Limousin P, Ling H, Lewis P, Proukakis C, Quinn N, Lees AJ, Hardy J, Revesz T, Houlden H, Holton JL (2013) α-Synucleinopathy associated with G51D SNCA mutation: a link between Parkinson's disease and multiple system atrophy? Acta Neuropathol 125:753–769.

Kiely AP, Ling H, Asi YT, Kara E, Proukakis C, Schapira AH, Morris HR, Roberts HC, Lubbe S, Limousin P, Lewis PA, Lees AJ, Quinn N, Hardy J, Love S, Revesz T, Houlden H, Holton JL (2015) Distinct clinical and neuropathological features of G51D SNCA mutation cases compared with SNCA duplication and H50Q mutation. Mol Neurodegener 10:41.

Kim S, Yun SP, Lee S, Umanah GE, Bandaru VV, Yin X, Rhee P, Karuppagounder SS, Kwon SH, Lee H, Mao X, Kim D, Pandey A, Lee G, Dawson VL, Dawson TM, Ko HS (2018) GBA1 deficiency negatively affects physiological α-synuclein tetramers and related multimers. Proc Natl Acad Sci USA 115:798–803.

Krüger R, Kuhn W, Müller T, Woitalla D, Graeber M, Kösel S, Przuntek H, Epplen JT, Schöls L, Riess O (1998) Ala30Pro mutation in the gene encoding alpha-synuclein in Parkinson's disease. Nat Genet 18:106–108.

Lesage S, Anheim M, Letournel F, Bousset L, Honoré A, Rozas N, Pieri L, Madiona K, Dürr A, Melki R, Verny C, Brice A, French Parkinson's Disease Genetics Study Group (2013) G51D α-synuclein mutation causes a novel parkinsonian-pyramidal syndrome. Ann Neurol 73:459–471.

Liu H, Koros C, Strohäker T, Schulte C, Bozi M, Varvaresos S, Ibáñez de Opakua A, Simitsi AM, Bougea A, Voumvourakis K, Maniati M, Papageorgiou SG, Hauser AK, Becker S, Zweckstetter M, Stefanis L, Gasser T (2021) A novel SNCA A30G mutation causes familial Parkinson's disease. Mov Disord 36:1624–1633.

Maroteaux L, Campanelli JT, Scheller RH (1988) Synuclein: a neuron-specific protein localized to the nucleus and presynaptic nerve terminal. J Neurosci 8:2804–2815.

Mhyre TR, Boyd JT, Hamill RW, Maguire-Zeiss KA (2012) Parkinson's disease. Subcell Biochem 65:389–455.

Nalls MA, Pankratz N, Lill CM, Do CB, Hernandez DG, Saad M, DeStefano AL, Kara E, Bras J, Sharma M, Schulte C, Keller MF, Arepalli S, Letson C, Edsall C, Stefansson H, Liu X, Pliner H, Lee JH, Cheng R, et al. (2014) Large-scale meta-analysis of genome-wide association data identifies six new risk loci for Parkinson's disease. Nat Genet 46:989–993.

Nemani VM, Lu W, Berge V, Nakamura K, Onoa B, Lee MK, Chaudhry FA, Nicoll RA, Edwards RH (2010) Increased expression of alpha-synuclein reduces neurotransmitter release by inhibiting synaptic vesicle reclustering after endocytosis. Neuron 65:66–79.

Newberry RW, Leong JT, Chow ED, Kampmann M, DeGrado WF (2020) Deep mutational scanning reveals the structural basis for α-synuclein activity. Nat Chem Biol 16:653–659.

Nicholatos JW, Groot J, Dhokai S, Tran D, Hrdlicka L, Carlile TM, Bennion M, Dalkilic-Liddle I, Hirst WD, Weihofen A (2021) SCD inhibition protects from alpha synuclein induced neurotoxicity but is toxic to early neuron cultures. eNeuro 8:ENEURO.0166-21.2021.

Nuber S, Nam AY, Rajsombath MM, Cirka H, Hronowski X, Wang J, Hodgetts K, Kalinichenko LS, Müller CP, Lambrecht V, Winkler J, Weihofen A, Imberdis T, Dettmer U, Fanning S, Selkoe DJ (2021) A stearoyl-coenzyme A desaturase inhibitor prevents multiple Parkinson disease phenotypes in α-synuclein mice. Ann Neurol 89:74–90.

Nuber S, Rajsombath M, Minakaki G, Winkler J, Müller CP, Ericsson M, Caldarone B, Dettmer U, Selkoe DJ (2018) Abrogating native α-synuclein tetramers in mice causes a L-DOPA-responsive motor syndrome closely resembling Parkinson's disease. Neuron 100:75–90.e5.

Pandey N, Schmidt RE, Galvin JE (2006) The alpha-synuclein mutation E46K promotes aggregation in cultured cells. Exp Neurol 197:515–520.

Pasanen P, Myllykangas L, Siitonen M, Raunio A, Kaakkola S, Lyytinen J, Tienari PJ, Pöyhönen M, Paetau A (2014) Novel α-synuclein mutation A53E associated with atypical multiple system atrophy and Parkinson's disease-type pathology. Neurobiol Aging 35:2180.e1–5.

Perlmutter JD, Braun AR, Sachs JN (2009) Curvature dynamics of alpha-synuclein familial Parkinson disease mutants: molecular simulations of the micelle- and bilayer-bound forms. J Biol Chem 284:7177–7189.

Polymeropoulos MH, Lavedan C, Leroy E, Ide SE, Dehejia A, Dutra A, Pike B, Root H, Rubenstein J, Boyer R, Stenroos ES, Chandrasekharappa S, Athanassiadou A, Papapetropoulos T, Johnson WG, Lazzarini AM, Duvoisin RC, Di Iorio G, Golbe LI, Nussbaum RL (1997) Mutation in the alpha-synuclein gene identified in families with Parkinson's disease. Science 276:2045–2047.

Proukakis C, Dudzik CG, Brier T, MacKay DS, Cooper JM, Millhauser GL, Houlden H, Schapira AH (2013) A novel α-synuclein missense mutation in Parkinson disease. Neurology 80:1062–1064.

Prusiner SB, Woerman AL, Mordes DA, Watts JC, Rampersaud R, Berry DB, Patel S, Oehler A, Lowe JK, Kravitz SN, Geschwind DH, Glidden DV, Halliday GM, Middleton LT, Gentleman SM, Grinberg LT, Giles K (2015) Evidence for α-synuclein prions causing multiple system atrophy in humans with parkinsonism. Proc Natl Acad Sci USA 112:E5308–E5317.

Ramalingam N, Dettmer U (2021) Temperature is a key determinant of alpha- and beta-synuclein membrane interactions in neurons. J Biol Chem 296:100271.

Rovere M, Powers AE, Jiang H, Pitino JC, Fonseca-Ornelas L, Patel DS, Achille A, Langen R, Varkey J, Bartels T (2019) E46K-like α-synuclein mutants increase lipid interactions and disrupt membrane selectivity. J Biol Chem 294:9799–9812.

Shahmoradian SH, Lewis AJ, Genoud C, Hench J, Moors TE, Navarro PP, Castaño-Díez D, Schweighauser G, Graff-Meyer A, Goldie KN, Sütterlin R, Huisman E, Ingrassia A, Gier Y, Rozemuller AJ, Wang J, Paepe AD, Erny J, Staempfli A, Hoernschemeyer J, et al. (2019) Lewy pathology in Parkinson's disease consists of crowded organelles and lipid membranes. Nat Neurosci 22:1099–1109.

Shi X, Li J, Zou X, Greggain J, Rødkær SV, Færgeman NJ, Liang B, Watts JL (2013) Regulation of lipid droplet size and phospholipid composition by stearoyl-CoA desaturase. J Lipid Res 54:2504–2514.

Simón-Sánchez J, Schulte C, Bras JM, Sharma M, Gibbs JR, Berg D, Paisan-Ruiz C, Lichtner P, Scholz SW, Hernandez DG, Krüger R, Federoff M, Klein C, Goate A, Perlmutter J, Bonin M, Nalls MA, Illig T, Gieger C, Houlden H, et al. (2009) Genome-wide association study reveals genetic risk underlying Parkinson's disease. Nat Genet 41:1308–1312.

Singleton AB, Farrer M, Johnson J, Singleton A, Hague S, Kachergus J, Hulihan M, Peuralinna T, Dutra A, Nussbaum R, Lincoln S, Crawley A, Hanson M, Maraganore D, Adler C, Cookson MR, Muenter M, Baptista M, Miller D, Blancato J, et al. (2003) alpha-Synuclein locus triplication causes Parkinson's disease. Science 302:841.

Terry-Kantor E, Tripathi A, Imberdis T, LaVoie ZM, Ho GP, Selkoe D, Fanning S, Ramalingam N, Dettmer U (2020) Rapid alpha-synuclein toxicity in a neural cell model and its rescue by a stearoyl-CoA desaturase inhibitor. Int J Mol Sci 21:5193.

Theillet FX, Binolfi A, Bekei B, Martorana A, Rose HM, Stuiver M, Verzini S, Lorenz D, van Rossum M, Goldfarb D, Selenko P (2016) Structural disorder of monomeric α-synuclein persists in mammalian cells. Nature. Nature 530:45–50.

Vincent BM, Tardiff DF, Piotrowski JS, Aron R, Lucas MC, Chung CY, Bacherman H, Chen YQ, Pires M, Subramaniam R, Doshi DB, Sadlish H, Raja WK, Solís EJ, Khurana V, Le Bourdonnec B, Scannevin RH, Rhodes KJ (2018) Inhibiting stearoyl-CoA desaturase ameliorates α-synuclein cytotoxicity. Cell Rep 25:2742–2754.

Volles MJ, Lansbury PT (2007) Relationships between the sequence of alpha-synuclein and its membrane affinity, fibrillization propensity, and yeast toxicity. J Mol Biol 366:1510–1522.

Walker DG, Lue LF, Adler CH, Shill HA, Caviness JN, Sabbagh MN, Akiyama H, Serrano GE, Sue LI, Beach TG, Arizona Parkinson Disease Consortium (2013) Changes in properties of serine 129 phosphorylated α-synuclein with progression of Lewy-type histopathology in human brains. Exp Neurol 240:190–204.

Wang L, Das U, Scott DA, Tang Y, McLean PJ, Roy S (2014) α-Synuclein multimers cluster synaptic vesicles and attenuate recycling. Curr Biol 24:2319–2326.

Wang W, Perovic I, Chittuluru J, Kaganovich A, Nguyen LT, Liao J, Auclair JR, Johnson D, Landeru A, Simorellis AK, Ju S, Cookson MR, Asturias FJ, Agar JN, Webb BN, Kang C, Ringe D, Petsko GA, Pochapsky TC, Hoang QQ (2011) A soluble α-synuclein construct forms a dynamic tetramer. Proc Natl Acad Sci USA 108:17797–17802.

Weinreb PH, Zhen W, Poon AW, Conway KA, Lansbury PT (1996) NACP, a protein implicated in Alzheimer's disease and learning, is natively unfolded. Biochemistry 35:13709–13715.

Westphal CH, Chandra SS (2013) Monomeric synucleins generate membrane curvature. J Biol Chem 288:1829–1840.

Wise-Scira O, Dunn A, Aloglu AK, Sakallioglu IT, Coskuner O (2013) Structures of the E46K mutant-type α-synuclein protein and impact of E46K mutation on the structures of the wild-type α-synuclein protein. ACS Chem Neurosci 4:498–508.

Xu L, Bhattacharya S, Thompson D (2019) On the ubiquity of helical α-synuclein tetramers. Phys Chem Chem Phys 21:12036–12043.

Ysselstein D, Joshi M, Mishra V, Griggs AM, Asiago JM, McCabe GP, Stanciu LA, Post CB, Rochet JC (2015) Effects of impaired membrane interactions on α-synuclein aggregation and neurotoxicity. Neurobiol Dis 79:150–163.

Zarranz JJ, Alegre J, Gómez-Esteban JC, Lezcano E, Ros R, Ampuero I, Vidal L, Hoenicka J, Rodriguez O, Atarés B, Llorens V, Gomez Tortosa E, del Ser T, Muñoz DG, de Yebenes JG (2004) The new mutation, E46K, of alpha-synuclein causes Parkinson and Lewy body dementia. Ann Neurol 55:164–173.

Zhou J, Broe M, Huang Y, Anderson JP, Gai WP, Milward EA, Porritt M, Howells D, Hughes AJ, Wang X, Halliday GM (2011) Changes in the solubility and phosphorylation of α-synuclein over the course of Parkinson's disease. Acta Neuropathol 121:695–704.